2021-04-26

Tectonic Geomorphology of the Yatagan Fault (Mugla, SW Turkey): Implications for Quantifying Vertical Slip Rates along Active Normal Faults

Basmenji, M

10.3906/yer-2010-11
TURKISH JOURNAL OF EARTH SCIENCES
The Scientific and Technological Research Council of Turkey (TUBITAK-ULAKBIM)

Tectonic geomorphology of the Yatağan Fault (Muğla, SW Turkey): implications for quantifying vertical slip rates along active normal faults

Mehran BASMENJI[1, *], Taylan SANÇAR[2], Aynur DİKBAŞ[3],

Sarah J. BOULTON[4], Hüsnü Serdar AKYÜZ[1]

[1]Department of Geological Engineering, Faculty of Mines, İstanbul Technical University, İstanbul, Turkey

[2] Department of Geography, Munzur University, Tunceli, Turkey

[3] Department of Geological Engineering, Faculty of Engineering, İstanbul University-Cerrahpaşa, İstanbul, Turkey

[4] School of Geography, Earth and Environmental Sciences, University of Plymouth, Plymouth, UK

*Correspondence: basmenji17@itu.edu.tr

ORCIDs:

Mehran BASMENJI: https://orcid.org/0000-0001-9855-7533

Taylan SANÇAR: https://orcid.org/0000-0002-2500-9787

Aynur DİKBAŞ: https://orcid.org/0000-0003-4614-9399

Sarah J. BOULTON: https://orcid.org/0000-0002-8251-0025

Hüsnü Serdar AKYÜZ: https://orcid.org/0000-0001-9485-2017

Cite as: Basmenji M, Sançar T, Dikbaş A, Boulton SJ, Akyüz HS. Tectonic geomorphology of the Yatağan Fault (Muğla, SW Turkey): implications for quantifying vertical slip rates along active normal faults. Turkish Journal of Earth Sciences. doi: 10.3906/yer-2010-11

Abstract: South western Anatolia is dominated by E-W and NW-SE trending active faults. The dip-slip Yatağan Fault is one of these active structures that trends in a NW direction for ~30 km. To assess the relative tectonic activity of the Yatağan Fault, two geomorphic segments were defined along the fault: the FS-1 (northern segment) and the FS-2 (southern segment). The vertical slip rate pattern of the fault was analyzed using steepness indexes, chi (χ) plots, and log-log slope area graphs. Results of the analyses indicate that the steepness of the streams draining the footwall reveal increasingly higher values downstream along the fault. All of the main basins contain at least one slope-break knickpoint associated with tectonic uplift. Facet morphology-based investigations using empirical methods along faceted spurs of the Yatağan Fault indicate vertical slip rates of 0.16 ± 0.05 mm/yr and 0.3 ± 0.05 mm/yr for the FS-1 and the FS-2, according to relationship of facet slope angle (R_{sa}). Additionally, using the facet basal height relationship (R_{bh}) we calculated slip rates of 0.24 mm/yr and 0.36 mm/yr for the FS-1 and the FS-2 segments, respectively. Mountain front sinuosity analysis yields values of 1.34 and 1.2, while the ratio of valley-floor width to valley height gives values of 0.64 and 0.24 for the FS-1 and the FS-2 respectively, indicating typical active mountain front where the uplift rates are ≥ 0.5 mm/yr. Hypsometric analysis suggest a transition from mature to older stage for catchments along the Yatağan Fault. Comprehensive interpretation of the results from morphometric analysis, vertical slip rate calculations, and data based on field observations suggest preponderance of tectonic activity over erosional process along the Yatağan Fault. Our analyses reveal that the rate of the tectonic activity gradually increases from the FS-1 to the FS-2 along the fault.

Keywords: Tectonic geomorphology, normal fault, Yatağan Fault, slip rate, triangular facet, SW Anatolia

1. Introduction

The increasing usage of geomorphological markers by scientists has become an effective way to quantify rates and patterns of tectonic uplift in actively deforming landscapes (Wallace, 1978; Rockwell et al., 1985; Keller and Pinter, 1996; Wobus et al., 2006; Bull, 2008; Boulton and Whittaker, 2009; Pérez-Peña et al., 2010; Burbank and Anderson, 2013). The steep topography of the Earth's crust is associated with rapid uplift (Wobus et al., 2006). Generally, landscape morphology develops under the control of tectonics and various erosional processes. Hence, tectonic geomorphology can be used to quantify relative tectonic activity in erosional landscapes (Keller and Pinter, 1996).

Since active tectonics and erosional surface processes are interacting along fault-generated mountain fronts, geomorphic features are commonly used to interpret the deformation history of the region. Mountain fronts created by dip-slip faults have been studied by many geomorphologists since early 1900’s, such as investigations on mountain ranges of the Great Basin (Davis, 1903) and the Humboldt region in the USA (Louderback, 1904). Later studies include Bull and McFadden (1977), Wallace (1978), Bull (2008), DePolo and Anderson (2000), Keller and Pinter (2002), and Tsimi and Ganas (2015), developing different quantitative geomorphic tools, which provide important information about tectonic activity, uplift and denudation rates. Moreover, hills and fault-generated features along mountain fronts are also sensitive recorders of the long-term interaction between tectonic uplift and denudation (Wallace, 1978).

Drainage networks are another sensitive geomorphologic recorder of tectonic activity and erosional processes (Ouchi, 1985; Clark et al., 2005). The gradient and geometry of drainage systems are controlled by climatic changes, lithology, tectonics and denudation (Jackson and Leeder, 1994; Keller and Pinter, 1996; Schumm et al., 2002; Pérez-Peña et al., 2010; Burbank and Anderson, 2013). In particular, bedrock channel fluvial systems constitute sensitive

indicators of the relationship between relief, elevation, and denudation ratio (Howard and Kerby, 1983; Howard, 1994; Howard et al., 1994; Whipple and Tucker, 1999; Whipple, 2004). Integrated interpretation of the mountain front and the bedrock river profiles can be used to extract not only information related to ongoing tectonic deformation (e.g. uplift rates), but also provide insights into the past climate of the region (Snyder et al., 2000; Wobus et al., 2006; Anoop et al., 2013; Pan et al., 2015). Furthermore, they can be used to highlight potential active faults and relative tectonic activity between faults (Silva et al., 2003; Boulton and Whittaker, 2009; Kirby and Whipple, 2012; Yıldırım, 2014; Selçuk, 2016; Topal et al., 2016).

The current tectonic architecture of Western Anatolia is shaped by N-S trending rapid extension (Reilinger et al., 2006; Tur et al., 2015). Here, the total extension is distributed between the E-W trending horst-graben systems and the accompanying NW and NE striking structures (Şengör, 1987). The Yatağan Fault is one of the NW trending active structures of this system. The Yatağan Fault was studied previously (Atalay, 1980; Şaroğlu et al., 1987; Duman et al., 2011; Emre et al., 2013; Gürer et al., 2013), but its actual tectonic activity and its role in the morphologic evolution of the surrounding region have remained unclear. In addition, a dense population and growing civilization on and around this seismogenic zone are increasingly at risk from potential seismic activity along the Yatağan Fault. Paleoseismic investigations on the fault clearly indicate that the Yatağan Fault has been active during the Holocene period and has potential to generate surface rupturing earthquakes (Basmenji et al., 2020). Therefore, a critical step towards an improved understanding the seismic hazard of the Yatağan Fault is to study the tectonic geomorphology in order to determine the vertical slip rates and the pattern of associated tectonic deformation. In the framework of this study, our specific goals are; 1) to unravel the recent tectonic activity on Yatağan Fault by using various morphometric tools, 2) to estimate vertical slip rates based on mountain front generated

facets, and 3) to discuss the seismic hazard potential of the Yatağan Fault depending on morphometric analyses.

To assess the relative tectonic activity of the Yatağan Fault and investigate the seismic hazard potential, we combined new data from field observations with data obtained from different morphometric tools, which are sensitive to vertical movement. For this purpose, lithological units along the fault were classified based on their rock strength, then we applied channel profile analysis to interpret the landscape response to tectonic processes along the channels that drain in the footwall of the Yatağan Fault. Additionally, we analyzed the gradient and geometry of faceted spurs to estimate vertical slip rates on the Yatağan Fault. To quantify the rate of erosion and tectonic activity along mountain fronts generated by the Yatağan Fault, basic indices such as mountain-front sinuosity (S_{mf}) and ratio of valley-floor width to valley height (V_f) were applied. Finally, relationship between area and altitude (hypsometric analysis) of drainage basins were analyzed to assess the relative stages of the topographic evolution.

2. Regional setting

2.1. Neotectonic framework of the region

The regional tectonics of Anatolia is shaped by the convergence between the African, Arabian and Eurasian plates (McKenzie, 1972; Şengör and Yilmaz, 1981; Şengör et al., 1985; Dewey et al., 1989). This collision leads to initiation of two intra-continental shear zones: The North and East Anatolian Fault Zones. Following the generation of NAFZ (North Anatolian Fault Zone) and EAFZ (East Anatolian Fault Zone), the Anatolian microplate escaped towards the west owing to the contractional forces in the east (collision between the Arabian and Eurasian plates in Eastern Anatolia) and the Hellenic Trench slab-pull (subduction of the African plate beneath the Eurasian plate in Mediterranean region) in the west (Şengör et al, 1985; Allen et al., 2004; Reilinger, 2006). These interactions caused the

formation of four neotectonic provinces in Turkey, which are known as the Eastern Anatolian Compressional Province (EACP), the Central Anatolia 'Ova' Province (CAOP), The North Turkish Province (NTP), and the Western Anatolia Extensional Province (WAEP; Figure 1a). Since the middle Miocene, interactions between the NAFZ and the Hellenic Arc-Trench system governs the tectonic framework of the WAEP (Bozkurt, 2001; Reilinger et al., 2006). However, toward the southern parts of this extensional province, migration of the Hellenic Trench in S-SW direction (roll-back process) dominantly characterizes the tectonic framework and kinematics of this region (McKenzie, 1978; Dewey and Şengör, 1979; Le Pichon and Angelier, 1979; Şengör et al., 1985, 2005; Meulenkamp et al., 1988; Yilmaz et al., 2000; Reilinger et al., 2006). The E-W trending horst-graben systems, which resulted from N-S extension, characterize the general structural framework of the WAEP (Dumont et al., 1979; Şengör et al., 1985; Oral et al., 1995; Le Pichon et al., 1995).

Modern geodetic studies and micro-block modeling in the Aegean region (Barka and Reilinger, 1997; Kahle et al., 2000; Reilinger et al., 2006; Elitez et al., 2016; England et al., 2016) indicate that toward the SW of WAEP, the total strain is distributed between the E-W trending Büyük Menderes Graben, Gökova Fault Zone, and NW-trending fault systems. Focal mechanisms of major earthquakes indicate shallow hypocenter depth of up to 30 km and dominantly NNW-SSE extension regime (Figure 1b; Kiratzi and Louvari, 2003; Taymaz et al., 2004; Yolsal-Çevikbilen et al., 2014; CMT Harvard catalogue). Moreover, present-day GPS measurements suggest a gradually increasing trend of geodetic velocities from northern to southern parts of the SW Anatolia respectively (Figure 1b; Reilinger et al., 2006; England et al., 2016). Velocity variations between major boundaries (the Büyük Menderes Graben in the north, the Gökova Fault Zone in the south) of the region generates NW trending secondary faults (Reilinger et al., 2006; Elitez et al., 2016). These active faults are

dominantly characterized by an almost pure normal sense of slip (Bozkurt, 2001; Figure1 a&b).

2.2. The Yatağan Fault

The current N-S extension between Büyük Menderes Graben (BMG) and Gökova Fault Zone generates NW-SE trending secondary active structures in the southwestern part of Anatolia. The NE-dipping Yatağan Fault is one of those secondary structures. The Yatağan Fault has been the subject of a number studies since 1980. Initially, Atalay (1980) mapped the structure as a NE-dipping dip-slip fault, subsequently Şaroğlu et al. (1987) defined it as the northern part of the right lateral Muğla-Yatağan Fault zone. Eventually, Duman et al. (2011) and Emre et al. (2013) split the Muğla-Yatağan Fault zone into two individual faults, naming the NE-dipping part of the structure in the northwest as the Yatağan Fault for the first time; furthermore, they define the southeastern extension as the Muğla Fault owing to the change in the dip direction of the hanging wall to the SW (Karabacak, 2016; Basmenji et al., 2020). The fault geometry utilized in this study is compiled and simplified from Basmenji et al. (2020). Additionally, although the fault geometry utilized in the aforementioned study indicates a similar geometry to Emre et al. (2013) and Karabacak (2016)'s studies, it demonstrates different orientation especially along northern and southern ends (review Basmenji et al., 2020 for more details).

Structural analyses undertaken along the fault scarps and slickensides during the field investigations indicate the dominant normal sense of motion with the minor right-lateral strike-slip component as a result of NNE-SSW oriented extensional forces (Gürer et al., 2013; Basmenji at al., 2020). The fault trends for ~30 km between densely populated Yatağan and Muğla cities (Figure 2). The observed fault scarps steepen near to vertical (~80°NE) and forms sharp linear traces which are either morphologic or lithologic in origin. The morphologic traces are steep fault scarps in marble, colluvial aprons, and topographic

escarpments. The lithologic traces are formed due to stratigraphic separation and faulted strata. These faults were analyzed on digital elevation models (DEMs) derived by interpolation of 1:25.000 scale elevation contours with 10-m ground pixel resolution and Google Earth images. The lineations were also studied during field campaigns and mapped based on McCalpin (2009) and McClay (2013) criteria (e.g. direct observation of marble fault planes and stratigraphic separation along the fault; Basmenji et al., 2020).

The Yatağan Fault is subdivided into two geometric segments (FS-1 and FS-2) based on morphologic, geometric and orientation changes along the mountain fronts based on Bull (2008) and McCalpin's (2009) criteria of normal fault segmentation (Figure 2). The FS-1 segment has a length of ~10 km and characterized by two parallel/subparallel fault branches with a strike of N20°-30°W that extends between Yeniköy and Kapubağ villages. To the southeast, towards the Muğla city center, the FS-2 segment trends with a strike of N50°-60°W, bounds the SW margin of the Yatağan Basin and extends toward SE where it meets the Muğla Fault through a narrow valley with a complex orientation and geometry (Figure 1b; Basmenji et al., 2020). Steeply dipping escarpments (~80°NE) generate straight linear traces that form the mountain front of the highlands to the SW of Yatağan Basin. The other distinctive geomorphologic features are steep faceted spurs, fault breccia, fault-controlled slickensides, colluvial aprons, and deeply incised canyons which reflect the kinematic, geometry, and location of the fault.

Paleoseismologic investigations along the Yatağan Fault revealed destructive paleo-earthquake activity during the last 10,000 years and the potential to generate moderate to relatively strong earthquakes (Basmenji et al., 2020).

2.3. Geology of the Yatağan Fault and surrounding area

Quantifying tectonic activity with geomorphic markers partly depends on the relationship between lithological factors and erosional processes (El Hamdouni et al., 2008; Boulton and

Whittaker, 2009; Yıldırım, 2014). In terms of morphotectonic analysis, interpretation of results based on lithology is an important issue. To investigate the morphologic response to tectonic activity, the understanding of the local geology is significant, which affects the topography and morphometric indices as well.

The NW-SE trending Yatağan Basin lies unconformably on the metamorphic series of the Menderes Massif. Initiation of the terrestrial basin was in the lower-middle Miocene (Gürer and Yılmaz, 2002; Özer and Sözbilir, 2003; Gürer et al., 2013). Upper rock units of the Menderes Massif form the lithologic basement of the study area. The basement units are dominantly made up of Paleozoic-Mesozoic marble, phyllite and schist (Bozkurt and Park, 1994; Hetzel et al., 1998; Akbaş et al., 2011; Dora, 2011). The basement rock units such as the upper Paleozoic Phyllite (Pzfl) and Jurassic Cretaceous Marble (JKrmr) are dominantly exposed on the footwall block of Yatağan Fault (Figure 3). The Miocene terrigeneous clastics and carbonates composed of both fluvial and lake sediments (Eskihisar and Yatağan formations), unconformably overlie the metamorphic basement (Brinkmann, 1966; Şengör, 1980; Gürer and Yılmaz, 2002; Akbaş et al., 2011; Gürer et al., 2013). The Eskihisar and Yatağan Formations are mainly exposed on the hanging wall and footwall of the Yatağan Fault, respectively (Brinkmann, 1966; Atalay, 1980).

The terrigenous Eskihisar Formation (M1) unconformably lies on the basement units. This unit is Middle Miocene in age (Çağlayan et al., 1980) and is characterized by lake and fluvial sediments at the bottom (Figure 3). Starting from the base to upward, it contains gray-beige colored clays with high amount of mica, sand, and pebbles. There are sandy, clayey, sulphurous lignite interlayers within the clay sequences of this formation (Çağlayan et al.,1980; Gürer et al., 2013). Eskihisar Formation is unconformably covered by the Yatağan Formation (M2). The Yatağan Formation is predominantly made up of terrestrial fluvial deposits. Poorly-sorted conglomerates at the basement of the unit are covered by volcanic

tuff, silt, sandstone, claystone, marl, and limestone. Fining-upward and the presence of sandstone interlayers are the characteristic features of this formation (Çağlayan et al., 1980; Gürer et al., 2013). Quaternary deposits (Q; Figure 3) such as debris flows, alluvial fans, colluvial and fluvial deposits overlie all the older units in the study area (Akbaş et al., 2011). According to geological map, we observe that the Yatağan Fault mostly forms a boundary between the older and younger lithologic units along it's extent and forms a lithologic contact.

3. Methods

In this study, several geomorphic indices were utilized to quantify the tectonic activity along the Yatağan Fault in addition to field observations. The digital elevation model (DEM) produced from 1:25000 scale elevation contours, high-resolution satellite imagery served by Google Earth TM, field observations and previous studies are used in conjunction to analyze geomorphic features of the study area.

In terms of geomorphic approach, the indices which are sensitive to vertical deformation were determined. Some of these geomorphic markers are related to mountain front movements and others to drainage basin evolution. To understand the relationship between morphometric indices with geologic features of the area rock strength classification was additionally undertaken. The relative tectonic activity of the area has been studied with five main geomorphic indices. Those geomorphic indices are: 1- channel profile analysis, 2- facet morphology-based slip rates, 3- mountain-front sinuosity (S_{mf}), 4- the ratio of valley-floor width to valley height (V_f), 5- hypsometric curve and hypsometric integral (HI).

3.1. Rock strength

In terms of geomorphic analysis, the difference in hardness and resistance of lithologies can affect the morphologic evolution of the study area. Hence, it is crucial to evaluate rock strength classification of the region of interest to understand thoroughly the reaction of

morphologic features within the study area to different tectonic forces as suggested by similar studies (El Hamdouni et al., 2008; Alipoor et al., 2011; Yıldırım, 2014; Zondervan et al., 2020). In this study, during field campaigns quality and compaction of matrix-cement (resistance of constituent material and reinforcing matrix), rock type, and the ratio of resistance to the geologic pick blows and pocket knife cuts were investigated, since evaluations provide good proxies about the resistance of the different geologic units to erosional processes (Zondervan et al., 2020). Therefore, rock strength of different lithologies are characterized due to the number and intensity of hammer blows along with the scrape tests; moreover, particular lithologic units were classified into five different groups according to the basic rock strength descriptions of Selby (1980) and Goudie (2006). Then to confirm the accuracy of obtained results, the amassed rock strength data was examined and correlated with average mechanical rock strength measurements and classification of the metamorphic rocks that has conducted by Özbek et al. (2018) utilizing L and N-type Schmidt Hammer rebound values (review Table 1 for details).

3.2. Channel profile analysis

Study of channel networks is an essential issue to establish the effects of external forcing on the morphology (Burbank et al., 1996; Whipple, 2004; Wobus et al., 2006; Burbank and Anderson, 2013; Hurst et al., 2013). Numerical analysis of longitudinal stream profiles is an effective tool with which to discriminate the relationship between differential rock uplift rate and steady-state channel steepness and the transient response to changes in differential rock uplift in actively deforming landscapes (Kirby and Whipple, 2012). This method suggests that generally graded river profiles are well-described by a power-law relationship between local channel slope (S) and the contributing drainage area upstream (A) (Hack, 1973). Normalized channel steepness (k_{sn}) indexes is defined as:

$$S = k_{sn} A^{-\theta_{ref}}$$

Where S is the local channel gradient, k_{sn} is the normalized steepness index and θ_{ref} is the reference concavity (Whipple and Tucker, 1999; Kirby and Whipple, 2001, 2012; Wobus et al., 2006; Burbank and Anderson, 2013). Recent studies indicate strong empirical support for well-performing values of θ_{ref} between 0.4 and 0.5 in tectonically active regions; therefore, in this study best-fit value of θ_{ref} = 0.45 is used as suggested by various researchers (Snyder et al., 2000; Kirby and Whipple, 2001, 2012; Wobus, Crosby and Whipple, 2006; Hilley and Arrowsmith, 2008; Kirby and Whipple, 2012; DiBiase et al., 2010; Kent et al., 2017).

In tectonically active regions, the architecture of the bedrock channel profiles reflects erosional response to tectonic activity (Kirby and Whipple, 2012; Vanacker et al., 2015). Hovius (2000) classified the longitudinal bedrock channel profiles (based on their profile geometry) in three major categories: concave, concave-convex, and convex curves. Where concave profiles reflect the long-term balance between uplift and erosion rate, Concave-convex (S-shaped) profiles with erosional steps in the middle reaches represent long-term domination of erosional processes and convex profiles typically indicate areas where uplift is predominant (Hovius, 2000; Pérez-Peña et al., 2010).

In terms of river profiles, different lithologies, climate, tectonic forces and erosional processes or sediment deposition effectively control the incision rate of the steady-state river profiles and generates transient channel profiles, these modifications observed as elevation or gradient variations along channel profiles are known as knickpoints (Whipple and Tucker, 1999; Whipple, 2004; Kirby and Whipple, 2012). Typically morphology of knickpoints can be classified into two end-member morphologies: 1- vertical step and 2- slope break knickpoints (Haviv et al., 2010; Kirby and Whipple, 2012). Vertical-step knickpoints are mostly associated small-scale heterogeneities along river profile (e.g. lithological separation

along a fault) and record no significant evidence about the uplift trends of the region (Wobus, Crosby and Whipple, 2006; Kirby and Whipple, 2012; Boulton, 2020). Conversely, slope-break knickpoints develop because of abrupt increases in channel steepness along a river profile towards downstream direction as a result of sustained base-level fall potentially resulting from tectonic perturbation (Wobus et al., 2006; Kirby and Whipple, 2012). Tectonic forcing transforms river profile from steady-state to transient stage as a result in this change in the base-level (Kirby and Whipple, 2012). These differences allow the identification of differential rock uplift and initiation of previously unknown faults (Wobus et al., 2003; Wobus et al., 2005; Kirby and Whipple, 2012; Boulton, 2020). Thus, the analysis of slope-break knickpoints is critical to understand the pattern of regional-scale uplift (Wobus et al., 2006; Kirby and Whipple, 2012).

The longitudinal bedrock river profiles have been analyzed widely with the classical slope-area technique, however, this approach has some limitations (please refer to Perron and Royden, 2013 for details). To combat these issues related to topographic data Perron and Royden (2013) introduce a robust integral approach called chi (χ) plot. This approach is created based on stream-power law which utilizes elevation as a dependent variable to analyze both transient and steady-state longitudinal river profiles (Perron and Royden, 2013; Mudd et al., 2014). Practically, the chi (χ) technique integrates drainage basin area to overflow distance to transform the horizontal coordinate into chi (χ) space, which uses the dimensions of the distance between river outlet and position of the interest. The detailed explanation and calculation of chi (χ) derivation discussed thoroughly by several scientists (Harkins et al., 2007; Perron and Royden, 2013; Royden and Taylor Perron, 2013; Mudd et al., 2014), so we only provide the general form of the equation here:

$$\chi = \int_{x_b}^{x} \left(\frac{A_0}{A(x')} \right)^{\theta_{ref}} dx'$$

Where x_b is channel outlet (base level), x is the location of the desired position towards upstream direction, A is upstream drainage area, A_0 is reference scaling area, θ_{ref} is the reference concavity, and x' is a dummy variable (Kirby and Whipple, 2012; Perron and Royden, 2013; Willett et al., 2014; Forte and Whipple, 2018; Forte, 2019). In this study chi (χ) plots produced with parameters of A_0 = 1 km^2 (the best fit constant reference value to scale the chi (χ) axis; Whipple and Tucker, 1999; Perron and Royden, 2013) and θ_{ref} = 0.45 (as discussed earlier in this section). Therefore, with the given parameters a steady-state river profile transformed to chi (χ) space will appear as a straight line, that it's slope reflects the proportion of uplift rate to erosivity (Perron and Royden, 2013; Mudd et al., 2014). We employed chi (χ) plots along with slope-area analysis to identify the knickpoints of the main profiles and to discriminate the lithologic, erosional, and tectonic origin of the knickpoints and relative base level changes along associated channels, as these catchments cover almost all parts of the footwall block and are mature enough to represent the long-term interaction between tectonic uplift and erosivity with numerical methods. The TopoToolbox functions (Schwanghart and Scherler, 2014) and Matlab software were utilized to extract channel profiles, calculate steepness index (K_{sn}), and plotting chi (χ) profiles.

3.3. Facet morphology based slip rates

Triangular or trapezoid facets are one of the characteristic features of the normal fault morphology (Figure 4 a, b), and they form on the mountain-piedmont junction on the footwall of the normal faults (Wallace, 1978; Armijo et al., 1992; DePolo and Anderson, 2000; Caputo and Helly, 2005; Tsimi et al., 2007; Bull, 2008; Tsimi and Ganas, 2015). Development of mountain front facets along spur ridges reflects cumulative range-front uplift (Bull, 2008). Their slope evolution begins with ~60^o gradient and decreases rapidly through time as a result of erosional processes to 20^o - 30^o; besides, lithology, climate, and footwall

rock resistance are the other effective factors which play important roles on footwall uplift (Wallace, 1978; Tsimi and Ganas, 2015).

The main morphologic and geometric features of facets (facet slope and height) that provide fundamental information about fault slip rates and initiation of faulting were extracted from 1:25000 scale digital topographic maps and DEM utilizing zonal statistic tool in ArcGIS v.10.3.1 (Figure 4 c, d); additionally, as suggested by previous studies, the initiation of the faulting assumed to initiated in Miocene epoch (Gürer and Yılmaz, 2002). Therefore, in this study, to quantify slip rates since Miocene period we assumed a constant footwall uplift along the fault (Bull et al., 2006; Bull, 2008; Tsimi and Ganas, 2015); in addition, we considered long-term slip rates to provide valid vertical slip rates instead of short-term variations as suggested by Tsimi and Ganas (2015).

Tsimi and Ganas's (2015) empirical method focuses on the 232 triangular facets with an average slope of 20^{o} - 40^{o} along 10 active normal faults (with known slip rates ranging from ~ 0.2 mm/yr to ~ 0.8 mm/yr) in the Aegean-Mediterranean region. In our study, 20 facets along the Yatağan Fault represent a more gentle slope angle and possibly lower vertical slip rates compared to cases in the study of Tsimi and Ganas (2015). Therefore, their exponential equation that allows vertical slip assessment of normal faults with facet slope angles of lower than 20^{o} have utilized. For relation between facet slope angle and vertical slip rate they obtained:

$$Y = 0.0328e^{0.0938x}$$

Where Y represents the vertical slip rate (mm/yr), X is the facet slope angle in degree and e is the mathematical constant (Tsimi and Ganas, 2015).

DePolo and Anderson (2000) also developed an empirical method to estimate vertical slip rates based on the relationship between facet basal height and vertical slip rate. The authors studied 45 normal faults in Nevada (USA) with known slip rates. They classified faults in

three categories depending on their tectonic activity. Type-1 faults with active facets generally represent vertical slip rate of 0.1 mm/yr or higher. They obtained following relation for facet height and vertical slip rate for type-1 normal faults:

$Log_{10}\ S_v = 0.00248H - 0.938$

Where is S_v the vertical slip rate (mm/yr) and H is the maximum basal height of facet in meters. We applied this method to test and verify the vertical slip rates that we obtained by Tsimi and Ganas's (2015) method and as a second estimation. However, we focus on the Tsimi and Ganas's (2015) method to extrapolate vertical slip rates, as the analyzed normal faults in this study developed in more or less similar tectonic framework (at least in the Quaternary, the Hellenic subduction zone dominates the tectonic setting of Aegean Region) and long term climate conditions (at least since the late Quaternary) as the Yatağan fault.

3.4. Mountain-front sinuosity (S_{mf})

Mountain-front sinuosity reflects the different stages of equilibrium between tectonic uplift and erosion along mountain-piedmont junction (Bull and McFadden, 1977; Keller and Pinter, 1996; Silva et al., 2003; Bull, 2008). S_{mf} is defined as:

$S_{mf} = L_{mf} / L_s$

where L_{mf} represents the length of the topographic contour line in front of the mountain (the topographic break in the slope), and L_s indicate the actual distance between two ends of the same contour line (Bull and McFadden, 1977; Keller and Pinter, 1996; Silva et al., 2003). Young mountain fronts bounded by active faults, associated with greater tectonic uplift than erosion, tend to generate straight mountain-fronts, yielding lower values of S_{mf}. Whereas, cessation or reduction of the uplift and domination of the denudation processes along older mountain-fronts, generate sinuous and irregular mountain fronts with higher values of S_{mf}.

3.5. Ratio of valley-floor width to valley height (V_f)

To discriminate between broad, flat-floored U-shaped canyons and V-shaped valleys (Bull and McFadden, 1977; Keller and Pinter, 1996; Azor et al., 2002; Silva et al., 2003), the ratio of valley-floor width to valley height (V_f) index is applied along studied mountain fronts. V_f is defined as:

$V_f = 2V_{fw} / (E_{ld} - E_{sc}) - (E_{rd} - E_{sc})$

where V_{fw} is the width of the valley floor, E_{ld} and E_{rd} are the elevations of the left and right-hand valleys watersheds looking downstream, and E_{sc} is the elevation of the stream channel or valley floor. Lower values ($V_f < 1$) of V_f index represent, incised, V-shaped valleys, associated with domination of active uplift and lower rates of erosion. Whereas, higher rates ($V_f > 1$) of V_f denotes U-shaped, broad flat-floored canyons, and higher rates of erosional processes to tectonic uplift (Bull and McFadden, 1977; Rockwell, Keller and Johnson, 1985; Keller and Pinter, 1996; Silva et al., 2003; El Hamdouni et al., 2008; Pérez-Peña et al., 2010). To assess the tectonic activity, V_f index applied at a set distance of 0.2 to 1 km from the mountain front toward upstream for the studied 21 main valleys along the fault (Figure 5; Azor et al., 2002; Silva et al., 2003; Pérez-Peña et al., 2010).

3.6. Hypsometry

Hypsometric curves indicate the proportion of surface area over elevation of a catchment, while hypsometric integral represents the area below the hypsometric curve; thus, indicating the proportion of the basin that has not been eroded (Strahler, 1952; Keller and Pinter, 1996; El Hamdouni et al., 2008). Hypsometric integral (HI) can be calculated as:

$$HI = \frac{H_{mean} - H_{min}}{H_{max} - H_{min}}$$

where H_{mean}, H_{min}, and H_{max} represent the mean, minimum, and maximum elevation respectively (Pike and Wilson, 1971; Keller and Pinter, 1996). The geometry and

morphology of the hypsometric curve and the value of HI principally indicates the different stages of the topography and its geomorphic evolution. The rate of hypsometric integral remarkably decreases with the advance in geomorphic stage (Ohmori, 1993). Though, different rates of the HI are associated with state of erosional processes occurred in the whole catchment area and landform characteristics. HI values > 0.5 indicate strong influence of tectonic activity over erosivity and youthful stage of landscape evolution. By contrast, values HI values < 0.3 represent dominant control of erosion over tectonic uplift, and older landscapes. Moderate values between 0.3 and 0.5 depict mature stage of the topography and equilibrium between tectonic uplift and erosion (Ohmori, 1993; Keller and Pinter, 1996; El Hamdouni et al., 2008; Pérez-Peña et al., 2009a; Pérez-Peña et al., 2009b).

The shape of hypsometric curve indicates the erosional stage of the related basins. Moreover, the hypsometric curve plotted as function of normalized area and altitude, as a result of this function drainage basins of different sizes are comparable (Pérez-Peña et al., 2010). Geometric characteristic of hypsometric curves classified in three main categories, these are convex, S-shaped (concave-convex) and concave shaped curves (Pantosti et al., 1993; Keller and Pinter, 1996; Pérez□Peña et al., 2009a; Pérez-Peña et al., 2010; Giaconia et al., 2012). Convex hypsometric curves represent dominant tectonic activity and weak erosion; S-shaped curves depict moderate rate of erosion; and concave curves are correlated with higher rates of erosion (Keller and Pinter, 1996; Pérez□Peña et al., 2009c; Giaconia et al., 2012). However, there are also complex hypsometric curves that indicate rejuvenation of the related basins (Giaconia et al, 2012). In order to draw the hypsometric curves and calculate the hypsometric integral values of the catchments, CalHypso ArcGIS module (Pérez-Peña et al., 2009b) is used in this study.

4. Results

4.1. Rock strength

Implemented rock strength evaluations within the area indicate that the rock strength values for lithologic units varies from very low rock strength for Quaternary units (alluvium, colluvium, debris flows and fluvial deposits), low for Yatağan (M1) and Eskihisar (M2) Formations (lacustrine sediments and older fluvial deposits containing poorly consolidate clastics), moderate for phyllite (Pzfl), high for schist (TrJş, PKşq and Pzş), and very high for marble (JKrmr and Pmr; Figure 5; Table 1).

Rock strength investigations on different lithologies reflect that the footwall block along the Yatağan Fault mostly represents moderate to very high rock strength (Figure 5). Mountain fronts along the Yatağan Fault made up of marble, phyllite, and clastics that represent very high, moderate, and low strength respectively. In particular, the mountain front along the FS-1 segment is mostly characterized by moderate to low rock strength with partly very high rock strength, while the mountain front along the FS-2 is mostly characterized by very high strength (Figure 5).

4.2. Channel profile analysis

The river profile analysis is an excellent technique for analyzing the morphological pattern of a particular landscape. The spatial pattern of channel steepness indices ranges between 0 – 75 $m^{0.9}$ and 300 – 500 $m^{0.9}$ along the Yatağan Fault assuming a reference concavity of 0.45. It is conspicuous that the highest values are located at the southern parts of the footwall block (FS-2), while northern parts of the footwall block (FS-1) represent lower values (Figure 6 a, b). Even though channel steepness values represent a gradually increasing trend from the FS-1 toward the FS-2, some large steepness changes from 300 to 75 $m^{0.9}$ are observed along the FS-1, these abrupt falls mostly coinciding with orientation of the Yatağan Fault. This phenomenon is clearly observable along the mountain front of the FS-2 (Figure 6 a, b).

Channel steepness analysis indicate that sudden changes of steepness occur along the parts of the footwall block near mountain front, where stream channels drain from fault zone toward mountain piedmont junction where extreme changes in steepness contemplated.

The morphology of the longitudinal bedrock channel profiles was analyzed along the Yatağan Fault, and they mostly represent concave to S-shaped profiles. Across the FS-1 segment, most of the drainage basins (5, 6, 7, 8, 9, 11) represent concave profile geometry; on the contrary, basins 1, 2, 3, 4 represent linear to convex (S-shaped) geometry that have knickpoints. However, only drainage basin 10 indicates convex geometry along the FS-1. Along the FS-2 segment, drainage basins (13, 14, 18, 19, 20) dominantly represent convex geometry; in contrast, basins 16 and 17 represent concave-convex (S-shaped) geometry. Furthermore, the basins 12 and 15 exhibit concave geometry, and only basin 21 shows a significantly concave profile geometry. It is evident that the knickpoints along the longitudinal channel profiles are mainly coincident with abrupt changes in steepness.

Knickpoints along these profiles are the result of tectonic or erosional processes, or lithological factors of the area (Figure 3). In this study, only knickpoints associated with tectonic features are considered (Figure 7) and knickpoints associated with lithologic changes and/or other factors are not analysed further. In particular, abrupt changes in base level along basins 1, 2, 3, 5, 6, 14, 17, 18 and 19 correlated precisely with the position and/or geometry of the Yatağan Fault and pattern of the steepness changes along the mountain front (Figure 6 a, b).

Additionally, to evaluate morphological characteristics of the major knickpoints associated with main channel profiles, eight major drainage basins (basins 1, 6, 7, 9, 12, 14, 16, 21) were extracted along the axis of the Yatağan Fault. These basins drain the footwall with general trend of ENE-WSW and cross the fault along the mountain-piedmont junction. Longitudinal main channel profiles were plotted along with logarithmic gradient- area, chi (χ) - auto $k_{sn,}$

and chi (χ) - elevation plots with reference concavity value (θ_{ref}) of 0.45 to evaluate and interpret signals of tectonic forcing and topographic characteristics of the sudden changes of base-level along main channels within study area; thereby, rivers of different sizes, orientation, gradient, and elevation were probed to evaluate the pattern of tectonic uplift and erosion.

First off, as discussed earlier in this section, the main longitudinal profiles of the extracted basins were analyzed. Then tectonic, erosional, and lithologic source of the base level changes along these profiles investigated utilizing logarithmic slope-area, chi (χ) - auto ksn, and chi (χ) - elevation plots and abrupt changes in gradient which were originated by tectonics, are identified (Figure 8 a, b, c, d; slope-break knickpoints). In general, results show that the upstream portion of all channels are associated with low values of gradient and k_{sn} values range between 8.02 and 110.72 $m^{0.9}$ (Table 2 and Figures. S. 1, 2, 3, 4 – d to h). In contrast, the lower portions of the channels toward downstream direction represent higher range of gradient and k_{sn} values that range between 23.53 and 998.48 $m^{0.9}$. The results evidently reveal that all of predominant rivers that run through the axis of the fault contain at least one slope-break knickpoint, since these rivers are experiencing abrupt changes in steepness along their downstream distance (Figure 3; Table 2; Figures. S. 1, 2, 3, 4 - a to h).

4.3. Facet morphology based slip rates

Field observations, Google Earth and DEM investigations indicate the facets along the studied mountain fronts of the Yatağan Fault are dominantly triangular (Figure 4 a, b and Figure 9 a, b). The facet height and slope were measured for 20 facets along the Yatağan Fault and mean values calculated for each geometric segment. The slope values range between 12.09° and 32.06°, whereas facet heights range between 60 m and 285 m (Table 3). Then these values were used to estimate vertical slip rates with two empirical methods from

the relationship of triangular facet slope to basal height as mentioned before (Tsimi and Ganas, 2015; DePolo and Anderson, 2000).

The Tsimi and Ganas (2015)'s empirical method was implemented to facet spurs along the mountain front of the Yatağan Fault. This assessment represents vertical slip rates of 0.16 ± 0.05 mm/yr for the FS-1 and 0.3 ± 0.05 mm/yr for the FS-2 segments. Furthermore, the DePolo and Anderson (2000)'s empirical method was employed to examine the obtained results from the first method. The vertical slip rate estimation by this method is 0.24 mm/yr for the FS-1 and 0.36 mm/yr for the FS-2 which is quite similar to those obtained with the former method.

4.4. Mountain-front sinuosity (S_{mf})

The S_{mf} index was applied to the mountain-piedmont junction along the Yatağan Fault. This index is very effective for the investigation of the relationship between uplift and erosional processes. S_{mf} values are 1.34 and 1.2 for the FS-1 and the FS-2 respectively (Figure 5 and Table 4). These relatively low S_{mf} values indicate straight mountain fronts.

4.5. The ratio of valley-floor width to valley-height (V_f)

The calculated values of V_f along the FS-1 segment of Yatağan Fault range from 0.21 to 2.07. By contrast, along the FS-2 segment the values are confined to the range between 0.07 and 0.39 (Table 4 and Figure 5). Generally, average values of each segment 0.64 for the FS-1 and 0.24 for the FS-2 segment; consequently, some valleys along the FS-2 recorded relatively lower values compared to the FS-1 (Table 4). As a result, geometry and shape of the valleys along both segments are V-shaped with incising narrow floors.

4.6. Hypsometry

Hypsometric integral measurements yield values ranging from 0.318 to 0.646 for the FS-1, and from 0.365 to 0.761 along the FS-2 (Table 4 and Figure 5). The obtained values indicate

that the basins along the FS-1 are dominantly of the mature stage, while the basins associated with the FS-2 generally reflect youthful stage.

The geometric characteristics of the hypsometric curves indicate a transition from convex to concave stage (Figure 10 a, b, c, d, e). The drainage basins (basins 1, 3, 5, 7, 8 and 11) along the mountain front of the FS-1 segment have dominantly S-shaped hypsometric curves, reflecting moderate stages of erosion and maturity (Figure 10 a, c). In contrast, the drainage basins (basins 15, 17, 18, 19 and 20) associated with FS-2 are mostly characterized by complex hypsometric curves with convex shape. These curves possibly reflect the rejuvenation of the related basins along the mountain front of the FS-2. However, there are also some basins (basins 2, 4, and 10) along the FS-1 with similar geometry (Figure 10 a, e). In addition, drainage basins 6 and 9 along the FS-1, and 12, 16, and 21 along the FS-2, covering the central and western parts of the footwall, yield concave hypsometric curves. These basins are associated with mature-older stages (Figure 10 a, b), yet despite that convex hypsometric curves (basins 13 and 14) representing youthful stage lie along the FS-2 segment of Yatağan Fault (Figure 10 a, d).

5. Discussion

To assess the tectonic activity of the Yatağan Fault with geomorphic tools, results are considered and interpreted separately for each segment. Longitudinal channel profiles along the Yatağan Fault represent a transition from concave to convex geometry from the FS-1 toward the FS-2. Tectonically-generated knickpoints along these profiles were detected and morphological features of the major knickpoints along mature channels were evaluated with steepness index and chi (χ) plots. The increasing trend of steepness variations along the main profiles in a downstream direction indicate that these slope-break knickpoints are associated with rapid rock uplift along the Yatağan Fault (Table 2). Additionally, the knickpoints along the main channel profile of the youthful basins were examined during field studies, as these

abrupt changes are small and younger to be assessed with steepness index and classical slope-area analysis. In particular, due to significant topographic anomalies along profiles 4, 18 and 19, related knickpoints were observed in the field (Figures 11 and 12). Field investigations indicate that along northern parts of the FS-1, knickpoints' structure are mainly controlled by the two parallel-subparallel branches of the Yatağan Fault (Figures 2 and 3), the fault within this area represents a lithologic contact between Mesozoic marble and Miocene clastics (Yatağan Formation). Evaluation of the morphologic anomalies along drainage basins 2, 3 and 4 (Figure 5) reveal that these basins are controlled by steeply dipping normal faults (~80^{o}) which generate differentiation in base level, slope, and elevation along the bedrock river profiles of the related basins (Figure 11 a, b, c, d). Moreover, observations through the FS-2 suggest that the abrupt changes in steepness along the bedrock river profiles of drainage basins (especially basins 18 and 19) along this segment, similarly developed by the steep normal fault scarps (dip of ~85^{o}) as a result of rapid uplift and sudden changes in base-level (Figure 12 a, b, c). The fault in this area split the Mesozoic marble from debris flows and colluvial deposits and bounds the western margin of the Yatağan Basin. Correlation of longitudinal stream profiles with channel steepness analysis and field observation indicates a good consistency, especially for knickpoints identified along the drainages 1, 2, 3, 4, 6, 7, 9, 12, 14, 16, 18 and 19. By and large, k_{sn} values range between 75 and 300 $m^{0.9}$ along the Yatağan Fault and indicate higher values and greater anomalies toward the southern parts of the fault (FS-2; Figure 6 a, b; Figures. S1, 2, 3, 4 - e and f). In addition, rock strength investigations indicate that most of the abrupt steepness variations mainly generated as a result of rapid uplift, and develop relatively insensitive from regional geology (Figures 3 and 6b).

Morphological properties of the triangular facets used to estimate vertical slip rates along the Yatağan Fault and two empirical methods employed for this purpose. The results of

morphometric analysis following the method proposed by Tsimi and Ganas (2015) represent vertical slip rates of 0.16 ± 0.05 mm/yr for the FS-1 and 0.3 ± 0.05 mm/yr for the FS-2. DePolo and Anderson (2000)'s method suggests vertical slip rates of 0.24 mm/yr for the FS-1 and 0.36 mm/yr for the FS-2, which are consistent with the former method's results.

To measure the relative long-term displacement between footwall and hanging wall of the Yatağan Fault, and to gain insights about the relationship and implications of topography with vertical slip rates, slope and deformation pattern, topographic profiles applied along two blocks parallel to the displacement direction (Kim and Sanderson, 2005; Yıldırım, 2014). Results indicate average vertical displacement of 207 m along the Yatağan Fault. In particular, investigations show that the higher displacement rates observed at the fault tips while the highest displacements are related to the southern tip (FS-2) of the Yatağan Fault with exact rates of 495 m and 423 m respectively (Figure 13). These data suggest that the topography effectively reflects the long-term displacement characteristics of the faults and provides information about the differential pattern of tectonic uplift (Kirby and Whipple, 2012; Yıldırım, 2014). Furthermore, in order to understand regional implications and relation of derived slip rates in regional scale in Anatolia, Greece, and Bulgaria we extrapolate the vertical slip rate results obtained with the Tsimi and Ganas's (2015) method and applied a regression solely with the outcomes of similar studies that have used the identical method to estimate vertical slip rates utilizing the faces slope angle along active normal faults with known slip rates (Figure 14; Tsimi and Ganas, 2015; Topal et al., 2016). Application of the regression with different normal faults located in different regions with a ranging of slip rates indicates that derived vertical slip rates for the Yatağan Fault are faster than the segment 1 & 5 of Akşehir Fault in Anatolia and the North Sparta Fault in southern Greece; in addition, these data are consistent with the Elovista and Kurpnik Faults in western Bulgaria and the Atalanti Fault in SW Greece (Figure 14). However, obtained vertical slip rates for the

Yatağan Fault indicate lower rates in contrast to the faults located in eastern, central and southern Greece. What is more, although Tsimi and Ganas (2015) used 30 m ASTER DEM data, the DEM data employed in this study was generated from 1:25000 scale topographic contours with 10 m interval; thereby, it provides a better resolution and more rigorous measurements for geomorphic analysis.

To discuss the relationship between erosional processes and tectonic uplift along mountain front of the Yatağan Fault, V_f and S_{mf} indices were analyzed. Results indicate 1.34 and 1.2 for S_{mf} and average value of 0.64 and 0.24 for V_f along the FS-1 and the FS-2 respectively which represent relative importance of tectonic uplift throughout the FS-2 (Table 4). However, rock strength classification indicates that an exceptional high V_f value of 2.07 along the FS-1 is associated with weak rock resistance (Figure 5 and Table 4). Except for some occasional high values, general trend of recorded values is consistent with each other. To quantify relative tectonic activity along mountain front, the correlation of S_{mf} and V_f values (standard deviations of the V_f values along both segments have been considered) has been applied (Bull and McFadden, 1977; Rockwell et al., 1985; Silva et al., 2003). The results of tectonic activity classification indicate high tectonic activity for both segments of the Yatağan Fault; besides, there is a good cohesion between the values of two indices along the mountain fronts (Figure 15). This classification also indicates > 0.5 mm/yr uplift rate along the Yatağan Fault.

The 21 drainage basins along the Yatağan Fault were analyzed with hypsometric curve and integral indices. The results of hypsometric integral indicate that most of the drainage basins (1, 2, 3, 5, 6, 7, 8, 9, 11) through the FS-1 represent mature stage, where the hypsometric integral values of these basins range mostly between 0.3 and 0.5. On the other hand, hypsometric integral values of the basins (12, 13, 14, 15, 17, 18, 19, 20) along the FS-2 are mainly > 0.5 and depict youthfully generated basin characteristics (Table 4). Moreover,

evaluation of results based on the rock strength of different lithologies states that the relatively lower values recorded along the FS-1 (basins 6 and 9) and the FS-2 (basins 12, 16 and 21) are particularly associated with rock resistance differentiation along both segments (Figure 5; Table 4). The hypsometric curve analysis indicates that most of the drainage basins along the mountain front of the footwall represent complex geometry. These irregular geometries with mostly convex trend are associated with rejuvenation of the related basins as a result of tectonic activity along the mountain front of the Yatağan Fault. For that reason, evaluation of these results suggests that even though the central and western parts of the footwall block along both segments represent older stages, yet topographic evolution along the FS-2 dominantly reflects youthful and rejuvenation stages. On the other hand, the FS-1 represents mature stage with some occasional rejuvenation processes along its extension. On the whole, from the western edges of the up thrown-block towards to the mountain front, the studied basins indicate transition from older to youthful stage.

As a result, geomorphic analyses by different methods indicate that the Yatağan Fault actively controls the geomorphologic evolution of the surrounding area. The tectonic uplift along the Yatağan Fault represents a gradual increase from the FS-1 to the FS-2. However, differential rock resistance associated with different lithologic units and karstic structures is other effective factors that shape the morphology of the surrounding area. Particularly, the catchment 21, which is located on Mesozoic marble, reflects karstic valley morphology. Hence, inferring its actual evolutional stage with hypsometric analysis could be a complicated issue.

Comprehensive combination of the results indicates that the FS-2 segment is more active compared to the FS-1 segment of the Yatağan Fault, and statistically represents a higher uplift rate and more steep topography. Besides, this segment represents a sharp morphology along its extension in the Yatağan Basin. According to the detailed geological map of the

area, the lithological properties may affect the uplift rates and results of the morphometric analyses. Detailed interpretation and combination of geological investigations by Backer-Platen (1970), Atalay (1980), Akbaş et al. (2011), Gürer et al. (2013) and our field studies indicate that the Mesozoic marble forms the basement of the area which represents very high rock strength to erosional processes. In comparison, other lithological units may have a local and lower influence on the geomorphologic evolution of the area. Overall, the FS-1segment indicates slightly lower vertical slip compared to the FS-2 segment; however, lower rates may be related to the local geologic and rock strength differentiation between two segments. In particular, the Miocene clastics (Eskihisar and Yatağan Formations) with low rock strength and Upper Paleozoic metamorphic rocks (phyllite) with moderate rock strength are dominant on the footwall of the FS-1. The Eskihisar Formation dominantly consists of clay, sand and pebbles, and the Yatağan Formation contains marl, claystone, sandstone and conglomerates. These formations unconformably lies on the metamorphic cover series of the Menderes Massif (Backer-Platen, 1970, Atalay, 1980). Based on the lithological properties of the FS-1 segment, it represents lower resistance to erosional processes in contrast to the FS-2 segment. On the other hand, karstic formations are the other factors, which mainly affect the geomorphic analyses of the neighboring regions of the FS-2 segment. It is tremendously challenging to distinguish the exact effect of karstic formations in implementing geomorphic analyses of the study area. However, weak rock strength of Yatağan and Eskihisar Formations and effective karstic subsidence on marble formations manipulates the morphometric indices results and tectonic activity classes of the related basins. Combination of field observations, recent seismic activity, morphometric analysis, and vertical slip rate estimations based on rock strength pattern of the area indicate that the FS-2 segment has higher tectonic uplift rate than the FS-1 segment.

Maximum earthquake magnitude (MAG) calculations performed by Basmenji et al. (2020) for the Yatağan Fault yield MAG = 6.6, which indicates that the Yatağan Fault has a potential to generate moderate to relatively strong and surface rupturing earthquakes in the future if the FS-1 and the FS-2 segments rupture together (Basmenji et al., 2020). Paleoseismological studies on the Yatağan Fault also revealed that at least one surface rupturing earthquake occurred on the fault during Holocene epoch (between 265 ± 95 BCE and 342 ± 131 CE; Basmenji et al., 2020). Moreover, the complexity of the tectonic setting of the area, the existence of other active structures around study area and relatively high extension rates of the region (~30 mm/yr based on Reilinger et al., 2006; Tur et al., 2015; England et al., 2016) in N-S direction are other evidence which support the magnitude estimation of 6 to 6.6 for the Yatağan Fault during relatively long intervals. Normal faults with a similar slip rate of 0.3 - 0.2 mm/yr can generate moderate to relatively strong earthquakes every few thousand years (Topal et al., 2016). However, growing urbanization and population rate on and around the Yatağan Fault increases the concerns about earthquake potential of the Yatağan Fault. Depending on comprehensive results from geomorphic, geologic, and paleoseismologic data, this study suggests that the Yatağan Fault has a potential to produce relatively strong earthquakes with relatively long intervals.

Last but not least, paleomagnetic studies are of utmost importance to understand the lateral switch and transference of deformation along dynamic spheres (Pueyo, 2010); thereby, in order to infer the implications of morphometric indices' outcomes in regional scale that has conducted with different morphometric indices, paleomagnetic data of former studies within the SW Anatolia domain investigated with scrutiny and matched with the outcomes of this study. By and large, amassed paleomagnetic data from previous studies indicate a general trend of counter clockwise rotation for the SW Anatolia region during Neogene period where the rotation rates yield a gradually increasing trend from 0 degree around its northern

boundary (Büyük Menderes Graben) to virtually -30 degree around its southern edge (Gökova Fault Zone; Kaymakcı et al., 2018). Additionally, culled and projected inclination angle values within the domain during the identical time span indicate an acute fall trend from about 52 degrees at the northwestern parts of the area to approximately 25 degrees toward the southeastern portion (Figure. S5; Kaymakcı et al., 2018). Hence, contemplating all the aforementioned outcomes of facet slope based vertical slip rates for both segments of the Yatağan Fault (0.16 mm/y for the Fs-1 and 0.3 for the Fs-2) and conducted former paleomagnetic studies (Kaymakcı et al., 2018) it is conspicuous that ascending pattern of the vertical slip rates and topography are emulating the pattern of the projected paleomagnetic inclination vector field and represents an intimate relation in terms of the variation of vertical motion throughout the segments (Figure. S5b). In particular, the FS-1 segment is approximately coinciding with the 0-0.15 degrees of the distance, whereas virtually the distance between 0.15-0.35 correspond to the FS-2 segment (Figure. S5b); in addition, the arising pattern of vertical slip rates from NW tip of the fault toward its SE margin represent an intimate relation with inclination profile of the area. Furthermore, margin between both segments which indicate the abrupt proliferated vertical slip rate pattern (from FS-1 to FS-2) is coinciding with the deviation angle of the profile between 0.15 and 0.20 degrees of distance which correspond to the boundary of the FS-1 and FS-2 as well. Therefore, although confined number of stations and data set within the area may affect the resolution of the contour lines and their interval, general morphotectonic pattern of the region is fairly coinciding with the frame of compiled and projected inclination values within the Neogene period.

6. Conclusions

The Yatağan Fault is mapped in detail during this study and linear mountain fronts and its geomorphic and geometric parameters analyzed with different tools in terms of tectonic geomorphology. To investigate the response of morphologic features to tectonic uplift and quantify the effects of the erosional processes, different geomorphic indices applied. Rock strength classification of the area along mountain fronts denotes mainly moderate to low rock strength in the FS-1 and dominantly very high rock strength for the FS-2. Results obtained from normalized channel steepness analysis range between 0-75 and 300-500 and the values rise from the FS-1 to the FS-2 segment where greater anomalies occur along the FS-2. Longitudinal topographic profiles of the streams indicate transition from concave to convex stage. Overall, stair steps along the longitudinal channel profiles represent a good correlation with steepness indice variations. Further, evaluations with chi (χ) plots along main basins indicate that these anomalies are slope-break knickpoints and associated with rapid rock uplift along the Yatağan Fault. Additionally, rock strength investigations indicate that abrupt anomalies are relatively insensitive to geological factors.

Facet slope based vertical slip rates indicate 0.16 ± 0.05 mm/yr for the FS-1 and 0.3 ± 0.05 mm/yr for the FS-2. Similarly, facet height based method suggest preferred vertical slip rates of 0.24 mm/yr for the FS-1 and 0.36 mm/yr for the FS-2. Comprehensively, in regional scale, obtained vertical slip rates are in intimate relation and harmony with normal faults from neighboring regions.

S_{mf} and V_f values indicate a linear mountain front with incising valleys for both segments. Correlation of S_{mf} and V_f values with tectonic activity classification indicate a good consistency and uplift rate of $\geq$ 0.5 mm/yr. Hypsometric curve and hypsometric integral denote that catchments along the footwall block of the Yatağan Fault are in transition from mature to young stage from the FS-1 to the FS-2 segment. Estimated rates are consistent with

the pattern of the morphology and results of the other geomorphic indexes. Furthermore, a comparison of topographic profiles along footwall and hanging wall of the Yatağan Fault shows 207 m of average vertical displacement.

Overall, obtained results from different morphometric analysis are consistent with each other and show a good correlation with the topography of the study area geodynamic evolution of the Aegean region. Generally, domination of tectonic activity increases from the FS-1 toward the FS-2 gradually. Combination of results from morphometric analysis including field observations indicates that the Yatağan Fault is effectively controlling the geomorphologic evolution of the area and has a potential to produce strong earthquakes in future.

Acknowledgments

This paper is a part of MSc thesis of the first author which was supported by Scientific and Technological Research Council of Turkey (TÜBİTAK; Project No: 116Y179). We are indebted to Dr. Marjan BASMENJI for enthusiastic financial and moral support. We are grateful to Dr. Turgay İŞSEVEN for critical supervision during projection and interpretation of paleomagnetic data which add exorbitant value to the first draft of the manuscript. We thank Müge YAZICI for helpful recommendations and suggestions regarding some indices especially hypsometry. We thank Dr. Cengiz ZABCI for encouragement and helpful discussions. We appreciate Erdem KIRKAN's valuable assistance during field studies. Ultimately, we are immensely thankful to three anonymous referees for their crucial critiques and feedbacks that have enhanced the first draft of the manuscript and added more regional dimension. Some of the figures in this paper are generated by Generic Mapping Tools (GMT; Wessel et al., 2013).

References

Akbaş B, Akdeniz N, Aksay A, Altun İ, Balcı V et al. (2011). Türkiye Jeoloji Haritası. Maden Tetkik ve Arama Genel Müdürlüğü Yayını. Ankara, Türkiye: Maden Tetkik ve Arama Genel Müdürlüğü (in Turkish).

Akkök R (1983). Structural and metamorphic evolution of the northern part of the Menderes massif: new data from the Derbent area and their implication for the tectonics of the massif. The Journal of Geology. University of Chicago Press 91 (3): 342–350.

Alipoor R, Poorkermani M, Zare M, El Hamdouni R (2011). Active tectonic assessment around Rudbar Lorestan dam site, High Zagros Belt (SW of Iran), Geomorphology. Elsevier 128 (1–2): 1–14.

Allen M, Jackson J, Walker R (2004). Late Cenozoic reorganization of the Arabia-Eurasia collision and the comparison of short-term and long-term deformation rates, Tectonics. Wiley Online Library 23 (2).

Anoop A, Prasad S, Krishnan R, Naumann R, Dulski P (2013). Intensified monsoon and spatiotemporal changes in precipitation patterns in the NW Himalaya during the early-mid Holocene, Quaternary International. Elsevier 313: 74–84.

Aral İ (1989). Geology of the Menderes Massif and the Lycian Nappes south of Denizli, western Taurides. Citeseer.

Armijo R, Lyon-Caen H, Papanastassiou D (1992). East-west extension and Holocene normal-fault scarps in the Hellenic arc, Geology. Geological Society of America 20 (6): 491–494.

Ashworth JR, Evirgen MM (1985a). Plagioclase relations in pelites, central Menderes Massif, Turkey. I. The peristerite gap with coexisting kyanite, Journal of Metamorphic Geology. Wiley Online Library 3 (3): 207–218.

Ashworth JR, Evirgen MM (1985b). Plagioclase relations in pelites, central Menderes

Massif, Turkey. II. Perturbation of garnet-plagioclase geobarometers, Journal of Metamorphic Geology. Wiley Online Library 3 (3): 219–229.

Atalay Z (1980). Stratigraphy of continental Neogene in the region of Muğla-Yatağan, Turkey. Geological Bulletin of Turkey 23: 93–99.

Azor A, Keller EA, Yeats RS (2002). Geomorphic indicators of active fold growth: South Mountain–Oak Ridge anticline, Ventura basin, southern California, Geological society of america bulletin. Geological Society of America 114 (6): 745–753.

Barka A, Reilinger R (1997). Active tectonics of the Eastern Mediterranean region: deduced from GPS, neotectonic and seismicity data.

Basmenji M, Akyüz HS, Kırkan E, Aksoy ME, Uçarkuş G et al. (2020). Earthquake history of the Yatağan Fault (Muğla, SW Turkey): implications for regional seismic hazard assessment and paleoseismology in extensional provinces. Turkish Journal of Earth Sciences (2021) 30: 161-181. doi: 10.3906/yer-2006-23

Başarır E (1970). Bafa gölünün doğusunda kalan Menderes Masifi güney kanadının jeolojisi ve petrografisi, EÜ Fen Fak. İlmi Raporları Serisi (102): 1–44.

Başarır E (1975). Çine Güneyindeki metamorfitlerin petrografisi ve bireysel indeks minerallerin doku içersindeki gelişimleri. Dsc Tezi, Ege Üniversitezi. İzmir, Lectorship thesis), Ege Üniversitesi YBI, Izmir (unpub-lished).

Benedetti L, Tapponnier P, King GC, Piccardi L (1998). Surface rupture of the 1857 southern Italian earthquake?, Terra Nova. Wiley Online Library 10 (4): 206–210.

Boulton SJ (2020). Geomorphic response to differential uplift: river long profiles and knickpoints from Guadalcanal and Makira (Solomon Islands), Frontiers in Earth Science. Frontiers 8: 10.

Boulton SJ, Whittaker AC (2009). Quantifying the slip rates, spatial distribution and evolution of active normal faults from geomorphic analysis: Field examples from an oblique-

extensional graben, southern Turkey, Geomorphology. Elsevier 104 (3–4): 299–316.

Bozkurt E (2001). Neotectonics of Turkey–a synthesis, Geodinamica acta. Taylor & Francis, 14 (1–3): 3–30.

Bozkurt E, Park LRG (1994). Southern Menderes Massif: an incipient metamorphic core complex in western Anatolia, Turkey, Journal of the Geological Society. Geological Society of London 151 (2): 213–216.

Brinkmann R (1966). Geotektonische Gliederung von Westanatolien, Neues Jahrbuch Geologie und Paleontogie Mh 10: 603–618.

Bull JM, Barnes PM, Lamarche G, Sanderson DJ, Cowie PA et al. (2006). High-resolution record of displacement accumulation on an active normal fault: implications for models of slip accumulation during repeated earthquakes. Journal of Structural Geology Elsevier 28 (7): 1146–1166.

Bull WB (2008). Tectonic geomorphology of mountains: a new approach to paleoseismology. John Wiley & Sons.

Bull WB, Mcfadden LD (1977). Tectonic geomorphology north and south of the Garlock Fault, California.

Burbank DW, Leland J, Fielding E, Anderson RS, Brozovic N et al. (1996). Bedrock incision, rock uplift and threshold hillslopes in the northwestern Himalayas, Nature. Nature Publishing Group 379 (6565): 505–510.

Burbank DW, Anderson RS (2013). Tectonic geomorphology. EEGS 1720 South Bellaire, Suite 110, Denver, CO 80222-4303, USA.

Burc Oral M, Reilinger R, Toksöz MN, King RW, Barka A et al. (1995). Global positioning system offers evidence of plate motions in eastern Mediterranean, EOS, Transactions American Geophysical Union. Wiley Online Library 76 (2): 9–11.

Çağlayan A, Öztürk E, Öztürk Z, Halit SA, Umur AK et al. (1980). Menderes Masifi

güneyine ait bulgular ve yapısal yorum. Jeoloji Mühendisliği Dergisi 4 (1): 9–18.

Caputo R, Helly B (2005). The Holocene activity of the Rodia fault, central Greece, Journal of Geodynamics. Elsevier 40 (2–3): 153–169.

Clark MK, Maheo G, Saleeby J, Farley KA (2005). The non-equilibrium landscape of the southern Sierra Nevada, California, GsA Today. The Geologıcal Society of America, Inc., 15 (9): 4.

Davis WM, university H (1903). The mountain ranges of the Great Basin.

DePolo CM, Anderson JG (2000). Estimating the slip rates of normal faults in the Great Basin, USA, Basin Research. Wiley Online Library 12 (3-4): 227–240.

Dewey JF, Helman ML, Knott SD, Turco E, Hutton DH (1989). Kinematics of the western Mediterranean, Geological Society, London, Special Publications. Geological Society of London 45 (1): 265–283.

Dewey JF, Şengör AMC (1979). Aegean and surrounding regions: complex multiplate and continuum tectonics in a convergent zone, Geological Society of America Bulletin. Geological Society of America 90 (1): 84–92.

DiBiase RA, Whipple KX, Heimsath AM, Ouimet WB (2010). Landscape form and millennial erosion rates in the San Gabriel Mountains, CA, Earth and Planetary Science Letters. Elsevier 289 (1–2): 134–144.

Dora OÖ (2011). Historical evolution of the geological researches in the Menderes massif, Maden Tetkik ve Arama Dergisi 142 (142): 1–23.

Duman TY, Emre Ö, Özalp S, Elmacı H (2011). 1: 250,000 Scale Active Fault Map Series of Turkey, Aydın (NJ 35-11) Quadrangle. General Directorate of Mineral Reserach and Exploration Publications. Ankara, Turkey: General Directorate of Mineral Research and Exploration.

Dumont JF, Uysal Ş, Şimşek Ş, Karamanderesi IH, Letouzey J (1979). Formation of the

grabens in southwestern Anatolia, Maden Tetkik ve Arama Dergisi. Citeseer 92: (92).

Dürr SH (1975). Über Alter und geotektonische Stellung des Menderes-Kristallins/SW-Anatolien und seine Aequivalente in der mittleren Aegaeis. Verlag nicht ermittelbar.

Elitez İ, Yaltırak C, Aktuğ B (2016). Extensional and compressional regime driven left-lateral shear in southwestern Anatolia (eastern Mediterranean): The Burdur-Fethiye Shear Zone, Tectonophysics. Elsevier 688: 26–35.

Emre Ö, Duman TY, Özalp S, Elmacı H, Olgun Ş et al. (2013). Açıklamalı Türkiye Diri Fay Haritası Ölçek 1/1.125.000. Maden Tetkik ve Arama Genel Müdürlüğü Yayını. Ankara, Turkey: Maden Tetkik ve Arama Genel Müdürlüğü (in Turkish).

England P, Houseman G, Nocquet J (2016). Constraints from GPS measurements on the dynamics of deformation in Anatolia and the Aegean, Journal of Geophysical Research: Solid Earth. Wiley Online Library 121 (12): 8888–8916.

Evirgen MM, Ataman G (1982). Etude du métamorphisme de la zone centrale du Massif de Menderes; Isogrades, pressions et température, Bulletin de la Société Géologique de France. Societe Geologique de France Paris, France 7 (2): 309–319.

Forte AM, Whipple KX (2018). Criteria and tools for determining drainage divide stability, Earth and Planetary Science Letters. Elsevier 493: 102–117.

Fortes AM (2019). The topographic analysis kit (TAK) for TopoToolbox, Earth Surface Dynamics 7 (1): 87.

Ganas A, White K (1996). Neotectonic fault segments and footwall geomorphology in Eastern Central Greece from Landsat TM data, Geological Society of Greece Special Publication 6: 169–175.

Giaconia F, Booth-Rea G, Martínez-Martínez JM, Azañón JM, Pérez-Peña JV et al. (2012). Geomorphic evidence of active tectonics in the Sierra Alhamilla (eastern Betics, SE Spain), Geomorphology. Elsevier 145: 90–106.

Goudie AS (2006). The Schmidt Hammer in geomorphological research, Progress in Physical Geography. Sage Publications Sage CA: Thousand Oaks, CA, 30 (6) pp. 703–718.

Gürer ÖF, Sanğu E, Özburan M, Gürbüz A, Sarica-Filoreau N (2013). Complex basin evolution in the Gökova Gulf region: implications on the Late Cenozoic tectonics of southwest Turkey, International Journal of Earth Sciences. Springer 102 (8): 2199–2221.

Gürer ÖF, Yılmaz Y (2002). Geology of the Ören and surrounding regions, SW Turkey. Turkish Journal of Earth Sciences 11: 2–18.

Hack JT (1973). Stream-profile analysis and stream-gradient index, Journal of Research of the us Geological Survey 1 (4): 421–429.

Hall J, Aksu AE, Elitez I, Yaltırak C, Çifçi G et al. (2014). The Fethiye–Burdur Fault Zone: a component of upper plate extension of the subduction transform edge propagator fault linking Hellenic and Cyprus Arcs, Eastern Mediterranean, Tectonophysics. Elsevier 635: 80–99.

El Hamdouni R, Irigaray C, Fernández T, Chacón J, Keller EA (2008). Assessment of relative active tectonics, southwest border of the Sierra Nevada (southern Spain). Geomorphology. Elsevier 96 (1–2): 150–173.

Harkins N, Kirby E, Heimsath A, Robinson R, Reiser U et al. (2007). Transient fluvial incision in the headwaters of the Yellow River, northeastern Tibet, China. Journal of Geophysical Research: Earth Surface. Wiley Online Library, 112(F3).

Haviv I, Enzel Y, Whipple KX, Zilberman E, Matmon A et al. (2010). Evolution of vertical knickpoints (waterfalls) with resistant caprock: Insights from numerical modeling, Journal of Geophysical Research: Earth Surface. Wiley Online Library, 115(F3).

Hetzel R, Romer RL, Candan O, Passchier CW (1998). Geology of the Bozdag area, central Menderes massif, SW Turkey: Pan-African basement and Alpine deformation. Geologische Rundschau. Springer 87 (3): 394–406.

Hilley GE, Arrowsmith JR (2008). Geomorphic response to uplift along the Dragon's Back

pressure ridge, Carrizo Plain, California, Geology. Geological Society of America 36 (5): 367–370.

Hovius N (2000). Macroscale process systems of mountain belt erosion, in Geomorphology and global tectonics. Wiley & Sons, pp. 77–105.

Howard AD (1994). A detachment-limited model of drainage basin evolution, Water resources research. Wiley Online Library 30 (7): 2261–2285.

Howard AD, Dietrich WE, Seidl MA (1994). Modeling fluvial erosion on regional to continental scales, Journal of Geophysical Research: Solid Earth. Wiley Online Library 99 (B7): 13971–13986.

Howard AD, Kerby G (1983). Channel changes in badlands, Geological Society of America Bulletin. Geological Society of America 94 (6): 739–752.

Hurst MD, Mudd SM, Yoo K, Attal M, Walcott R et al. (2013). Influence of lithology on hillslope morphology and response to tectonic forcing in the northern Sierra Nevada of California, Journal of Geophysical Research: Earth Surface. Wiley Online Library 118 (2): 832–851.

Jackson J, Leeder M (1994). Drainage systems and the development of normal faults: an example from Pleasant Valley, Nevada, Journal of Structural Geology. Elsevier 16 (8): 1041–1059.

Kahle HG, Cocard M, Peter Y, Geiger A, Reilinger R et al. (2000). GPS□derived strain rate field within the boundary zones of the Eurasian, African, and Arabian Plates. Journal of Geophysical Research: Solid Earth. Wiley Online Library 105 (B10): 23353–23370.

Karabacak V (2016). Seismic damage in the Lagina sacred area on the Mugla Fault: a key point for the understanding of the obliquely situated faults of western Anatolia. Journal of Seismology 20 (1): 277–289.

Kaymakcı N, Langereis C, Özkaptan M, Özacar AA, Gülyüz E et al. (2018). Paleomagnetic

evidence for upper plate response to a STEP fault, SW Anatolia, Earth and Planetary Science Letters. Elsevier 498: 101–115.

Keller EA, Pinter N (1996). Active tectonics. Prentice Hall Upper Saddle River, NJ.

Keller EA, Pinter N (2002). Active Tectonics: Upper Saddle River. Prentice Hall.

Kent E, Boulton SJ, Whittaker AC, Stewart IS, Alçiçek MC (2017). Normal fault growth and linkage in the Gediz (Alaşehir) Graben, Western Turkey, revealed by transient river long□ profiles and slope-break knickpoints, Earth Surface Processes and Landforms. Wiley Online Library 42 (5): 836–852.

Kim Y-S, Sanderson DJ (2005). The relationship between displacement and length of faults: a review, Earth-Science Reviews. Elsevier 68 (3–4): 317–334.

Kiratzi A, Louvari E (2003). Focal mechanisms of shallow earthquakes in the Aegean Sea and the surrounding lands determined by waveform modelling: a new database, Journal of Geodynamics. Elsevier 36 (1–2): 251–274.

Kirby E, Whipple K (2001). Quantifying differential rock-uplift rates via stream profile analysis, Geology. Geological Society of America 29 (5): 415–418.

Kirby E, Whipple KX (2012). Expression of active tectonics in erosional landscapes, Journal of Structural Geology. Elsevier 44: 54–75.

Louderback GD (1904). Basin Range structure of the Humboldt region, Bulletin of the Geological Society of America. Geological Society of America 15 (1): 289–346.

McCalpin JP (2009). Paleoseismology. Academic press.

McClay KR (2013). The mapping of geological structures. John Wiley & Sons.

McKenzie D (1972). Active tectonics of the Mediterranean region, Geophysical Journal International. Oxford University Press 30 (2): 109–185.

McKenzie D (1978). Active tectonics of the Alpine—Himalayan belt: the Aegean Sea and surrounding regions, Geophysical Journal International. Blackwell Publishing Ltd Oxford,

UK 55 (1): 217–254.

Meulenkamp JE, Wortel MJ, Van Wamel WA, Spakman W, Strating EH (1988). On the Hellenic subduction zone and the geodynamic evolution of Crete since the late Middle Miocene, Tectonophysics. Elsevier 146 (1–4): 203–215.

Mudd SM, Attal M, Milodowski DT, Grieve SW, Valters DA (2014). A statistical framework to quantify spatial variation in channel gradients using the integral method of channel profile analysis, Journal of Geophysical Research: Earth Surface. Wiley Online Library 119 (2): 138–152.

Ohmori H (1993). Changes in the hypsometric curve through mountain building resulting from concurrent tectonics and denudation, Geomorphology. Elsevier 8 (4): 263–277.

Ouchi S (1985). Response of alluvial rivers to slow active tectonic movement, Geological Society of America Bulletin. Geological Society of America 96 (4): 504–515.

Özbek A, Gül M, Karacan E, Alca Ö (2018). Anisotropy effect on strengths of metamorphic rocks, Journal of Rock Mechanics and Geotechnical Engineering. Elsevier 10 (1): 164–175.

Özer S, Sözbilir H (2003). Presence and tectonic significance of Cretaceous rudist species in the so-called Permo-Carboniferous Göktepe Formation, central Menderes metamorphic massif, western Turkey, International Journal of Earth Sciences. Springer 92 (3): 397–404.

Öztürk A, Koçyiğit A (1983). Menderes grubu kayalarının temel-örtü ilişkisine yapısal bir yak laşım (Selimiye-Muğla). Türkiye Jeoloji Kurumu Bülteni 26 (2): 99–106.

Pan B, Pang H, Zhang D, Guan Q, Wang L et al. (2015). Sediment grain-size characteristics and its source implication in the Ningxia–Inner Mongolia sections on the upper reaches of the Yellow River, Geomorphology. Elsevier 246: 255–262.

Pantosti D, Schwartz DP, Valensise G (1993). Paleoseismology along the 1980 surface rupture of the Irpinia fault: implications for earthquake recurrence in the southern Apennines, Italy, Journal of Geophysical Research: Solid Earth. Wiley Online Library 98 (B4): 6561–

6577.

Pérez-Peña JV, Azañón JM, Azor A, Tuccimei P, Della Seta M et al. (2009). Quaternary landscape evolution and erosion rates for an intramontane Neogene basin (Guadix–Baza basin, SE Spain). Geomorphology. Elsevier 106 (3–4): 206–218.

Pérez-Peña JV, Azor A, Azañón JM, Keller EA (2010). Active tectonics in the Sierra Nevada (Betic Cordillera, SE Spain): Insights from geomorphic indexes and drainage pattern analysis, Geomorphology. Elsevier 119 (1–2): 74–87.

Pérez-Peña JV, Azañón JM, Azor A (2009). CalHypso: An ArcGIS extension to calculate hypsometric curves and their statistical moments. Applications to drainage basin analysis in SE Spain, Computers & Geosciences. Elsevier 35 (6): 1214–1223.

Pérez□Peña JV, Azañón JM, Azor A, Delgado J, González-Lodeiro F (2009). Spatial analysis of stream power using GIS: SLk anomaly maps, Earth Surface Processes and Landforms. Wiley Online Library 34 (1): 16–25.

Perron JT, Royden L (2013). An integral approach to bedrock river profile analysis, Earth Surface Processes and Landforms. Wiley Online Library 38 (6): 570–576.

Le Pichon X, Chamot-Rooke N, Lallemant S, Noomen R, Veis G (1995). Geodetic determination of the kinematics of central Greece with respect to Europe: Implications for eastern Mediterranean tectonics, Journal of Geophysical Research: Solid Earth. Wiley Online Library 100 (B7): 12675–12690.

Le Pichon X, Angelier J (1979). The Hellenic arc and trench system: a key to the neotectonic evolution of the eastern Mediterranean area, Tectonophysics. Elsevier 60 (1–2): 1–42.

Picotti V, Ponza A, Pazzaglia FJ (2009). Topographic expression of active faults in the foothills of the Northern Apennines, Tectonophysics. Elsevier 474 (1–2): 285–294.

Pike RJ, Wilson SE (1971). Elevation-relief ratio, hypsometric integral, geomorphic area-altitude analysis, Geological Society of America Bulletin. Geological Society of America 82

(4): 1079–1084.

Pueyo EL (2010). Evaluating the paleomagnetic reliability in fold and thrust belt studies, Trabajos de Geologia, (30).

Reilinger R, McClusky S, Vernant P, Lawrence S, Ergintav S et al. (2006). GPS constraints on continental deformation in the Africa-Arabia-Eurasia continental collision zone and implications for the dynamics of plate interactions, Journal of Geophysical Research: Solid Earth. Wiley Online Library, 111(B5).

Rockwell TK, Keller EA, Johnson DL (1985). Tectonic geomorphology of alluvial fans and mountain fronts near Ventura, California, in Tectonic Geomorphology. Proceedings of the 15th Annual Geomorphology Symposium. Allen and Unwin Publishers, Boston, MA, pp. 183–207.

Royden L, Taylor Perron J (2013). Solutions of the stream power equation and application to the evolution of river longitudinal profiles, Journal of Geophysical Research: Earth Surface. Wiley Online Library 118 (2): 497–518.

Şaroglu F, Boray A, Emre O (1987). Active faults of Turkey, General Directorate of the Mineral Research and Exploration, Ankara, Turkey, 1(2), p. 0.

Satir M, Friedrichsen H (1986). The origin and evolution of the Menderes Massif, W-Turkey: a rubidium/strontium and oxygen isotope study, Geologische Rundschau. Springer 75 (3): 703–714.

Schumm SA, Schumm SA, Dumont JF, Holbrook JM (2002). Active tectonics and alluvial rivers. Cambridge University Press.

Schwanghart W, Scherler D (2014). TopoToolbox 2–MATLAB-based software for topographic analysis and modeling in Earth surface sciences, Earth Surface Dynamics. European Geosciences Union 2 (1): 1–7.

Selby MJ (1980). A rock mass strength classification for geomorphic purposes: with tests

from Antarctica and New Zealand, Zeitschrift für Geomorphologie Stuttgart 24 (1): 31–51.

Selçuk AS (2016). Evaluation of the relative tectonic activity in the eastern Lake Van basin, East Turkey, Geomorphology. Elsevier 270: 9–21.

Şengör AMC (1980). Türkiye'nin neotektoniğinin esasları, Türkiye Jeoloji Kurumu yayını, 40.

Şengör AMC (1987). Cross-faults and differential stretching of hanging walls in regions of low-angle normal faulting: examples from western Turkey, Geological Society, London, Special Publications. Geological Society of London 28 (1): 575–589.

Şengör AMC, Tüysüz O, Imren C, Sakınç M, Eyidoğan H, Görür et al. (2005). The North Anatolian fault: A new look, Annu. Rev. Earth Planet. Sci. Annual Reviews 33: 37–112.

Şengör AMC, Özeren MS, Keskin M, Sakınç M, Özbakır AD et al. (2008). Eastern Turkish high plateau as a small Turkic-type orogen: Implications for post-collisional crust-forming processes in Turkic-type orogens, Earth-Science Reviews. Elsevier 90 (1–2): 1–48.

Şengör AMC, Grall C, İmren C, Le Pichon X, Görür N et al. (2014). The geometry of the North Anatolian transform fault in the Sea of Marmara and its temporal evolution: implications for the development of intracontinental transform faults, Canadian Journal of Earth Sciences. NRC Research Press 51 (3): 222–242.

Şengör AMC, Görür N, Şaroğlu F (1985). Strike-slip faulting and related basin formation in zones of tectonic escape: Turkey as a case study. Special Publications of SEPM.

Sengör AMC, Satir M, Akkök R (1984). Timing of tectonic events in the Menderes Massif, western Turkey: Implications for tectonic evolution and evidence for Pan□African basement in Turkey, Tectonics. Wiley Online Library 3 (7): 693–707.

Şengör AMC, Yilmaz Y (1981). Tethyan evolution of Turkey: a plate tectonic approach, Tectonophysics. Elsevier 75 (3–4): 181–241.

Şengör AMC, Zabcı C (2019). The north Anatolian fault and the north Anatolian shear zone,

in Landscapes and landforms of Turkey. Springer, pp. 481–494.

Silva PG, Goy JL, Zazo C, Bardajı T (2003). Fault-generated mountain fronts in southeast Spain: geomorphologic assessment of tectonic and seismic activity, Geomorphology. Elsevier 50 (1–3): 203–225.

Snyder NP, Whipple KX, Tucker GE, Merritts DJ (2000). Landscape response to tectonic forcing: Digital elevation model analysis of stream profiles in the Mendocino triple junction region, northern California, Geological Society of America Bulletin. Geological Society of America 112 (8): 1250–1263.

Strahler AN (1952). Hypsometric (area-altitude) analysis of erosional topography, Geological Society of America Bulletin. Geological Society of America 63 (11): 1117–1142.

Strak V, Dominguez S, Petit C, Meyer B, Loget N (2011). Interaction between normal fault slip and erosion on relief evolution: Insights from experimental modelling, Tectonophysics. Elsevier 513 (1–4): 1–19.

Topal S, Keller E, Bufe A, Koçyiğit A (2016). Tectonic geomorphology of a large normal fault: Akşehir fault, SW Turkey, Geomorphology. Elsevier 259: 55–69.

Tsimi C, Ganas A, Ferrier G, Drakatos G, Pope RJ et al. (2007). Morphotectonics of the Sfakia normal fault, southwestern Crete, Greece, in Proceedings of 8th Pan-Hellenic Geographical Conference, pp. 4–7.

Tsimi C, Ganas A (2015). Using the ASTER global DEM to derive empirical relationships among triangular facet slope, facet height and slip rates along active normal faults, Geomorphology. Elsevier 234: 171–181.

Tur H, Yaltırak C, Elitez İ, Sarıkavak KT (2015). Pliocene–Quaternary tectonic evolution of the Gulf of Gökova, southwest Turkey, Tectonophysics. Elsevier 638: 158–176.

Vanacker V, Von Blanckenburg F, Govers G, Molina A, Campforts B et al. (2015). Transient river response, captured by channel steepness and its concavity, Geomorphology. Elsevier

228: 234–243.

Wallace RE (1978). Geometry and rates of change of fault-generated range fronts, north-central Nevada. Journal of Research of the U. S. Geological Survey 6 (5): 637–650.

Wessel P, Smith WH, Scharroo R, Luis J, Wobbe F (2013). Generic mapping tools: improved version released, Eos, Transactions American Geophysical Union. Wiley Online Library 94 (45): 409–410.

Whipple KX (2004). Bedrock rivers and the geomorphology of active orogens, Annu. Rev. Earth Planet. Sci. Annual Reviews 32: 151–185.

Whipple KX, Tucker GE (1999). Dynamics of the stream-power river incision model: Implications for height limits of mountain ranges, landscape response timescales, and research needs, Journal of Geophysical Research: Solid Earth. Wiley Online Library 104 (B8): 17661–17674.

Willett SD, McCoy SW, Perron JT, Goren L, Chen CY (2014). Dynamic reorganization of river basins, Science. American Association for the Advancement of Science 343 (6175).

Wobus C, Heimsath A, Whipple K, Hodges K (2005). Active out-of-sequence thrust faulting in the central Nepalese Himalaya, Nature. Nature Publishing Group 434 (7036): 1008–1011.

Wobus C, Whipple KX, Kirby E, Snyder N, Johnson J et al. (2006). Tectonics from topography: Procedures, promise, and pitfalls, Special papers-geological society of america. Boulder, Colo.; Geological Society of America; 1999, 398, p. 55.

Wobus CW, Crosby BT, Whipple KX (2006). Hanging valleys in fluvial systems: Controls on occurrence and implications for landscape evolution, Journal of Geophysical Research: Earth Surface. Wiley Online Library, 111(F2).

Wobus CW, Hodges K V, Whipple KX (2003). Has focused denudation sustained active thrusting at the Himalayan topographic front?, Geology. Geological Society of America 31 (10): 861–864.

Yilmaz Y, Genç ŞC, Gürer F, Bozcu M, Yilmaz K et al. (2000). When did the western Anatolian grabens begin to develop?, Geological Society, London, Special Publications. Geological Society of London 173 (1): 353–384.

Yıldırım C (2014). Relative tectonic activity assessment of the Tuz Gölü fault zone; Central Anatolia, Turkey, Tectonophysics. Elsevier 630: 183–192.

Zondervan JR, Stokes M, Boulton SJ, Telfer MW, Mather AE (2020). Rock strength and structural controls on fluvial erodibility: Implications for drainage divide mobility in a collisional mountain belt, Earth and Planetary Science Letters. Elsevier 538: 116221.

Zuchiewicz W, McCALPIN JP (2000). Geometry of faceted spurs on an active normal fault: case study of the Central Wasatch Fault, Utah, USA, in Annales Societatis Geologorum Poloniae.

Figure captions

Figure 1. a) Simplified neotectonic setting of the Turkey and surrounding area. Dashed line represents the proposed boundary between WAEP and CAOP (Şengör et al., 1985; 2014; Emre et al., 2013; Hall et al., 2014; Şengör and Zabcı, 2019). EACP: Eastern Anatolia Compressional Province, CAOP: Central Anatolia Ova Province, NTP: North Turkish Province, WAEP: Western Anatolia Extensional Province, NAFZ: North Anatolian Fault Zone, EAFZ: Eastern Anatolian Fault Zone, HT: Hellenic Trench, BMG: Büyük Menderes Graben, GFZ: Gökova Fault Zone, BFSZ: Burdur-Fethiye Shear Zone, CT: Cyprus Trench, MF: Muğla Fault. The dashed rectangular shows the location of the study area in Figure 1b. Topographic and bathymetric base maps are available at GEBCO data and products (GEBCO-GBD, 2019[1]). b) Seismotectonic map of the SW Turkey (faults from Emre et al., 2013). Small circles indicate seismic activity ($M_w \geq 2.5$) and are colored depending on their hypocenter depth between 1900 and 2020 (KOERI-EC, 2020[2]). Yellow and blue arrows indicate counterclockwise rotation relative to Eurasia (yellow and blue arrows are adopted from Reilinger et al., 2006 and England et al., 2016 respectively). Focal mechanisms of earthquakes that occurred during instrumental period (1965-2020) were compiled from Kiratzi and Louvari (2003) and CMT Harvard catalogue (2020)[3].

[1] GEBCO-GBD (2019). Gridded Bathymetry Data [online]. Website http://www.gebco.net /data_and_products/gridded_batymetry_data/ [accessed 11/2019].

[2] KOERI-EC (2020). Kandilli Earthquake Catalogue [online]. Website http://www.koeri. boun.edu.tr/sismo/zeqdb/ [accessed 03/2020].

[3] Global CMT Catalogue (2020). Global CMT Catalog Search [online]. Website https:// www.globalcmt.org/CMTsearch.html [accessed 03/2020].

Figure. 2 Seismotectonic map of the Yatağan Fault. Quaternary and active faults are compiled and simplified from Emre et al. (2013) and Basmenji et al. (2020). Blue arrows indicate the segment boundaries. Black circles show location of the modern cities and villages. The earthquake data is from KOERI-EC (2020[4]).

Figure 3. Simplified geologic map of the study area (compiled from Atalay, 1980; Akbaş et al., 2011; Gürer et al., 2013).

Figure 4. a) Simplified block diagram represents structural framework of a normal fault and related morphologic characteristics (inspired and modified after Wallace, 1978; Strak et al., 2011). b) Google Earth view of the faceted spurs along the Yatağan Fault and associated morphologic characteristics, H_f is the triangular facet basal height. c) Graphic shows the cross-section view of a triangular facet, Width: represent distance from top of facet to base, Height: is defined as the difference between maximum elevation and base elevation. d) Front aspect of a triangular facet on footwall of a normal fault. c & d adapted and modified after Tsimi and Ganas (2015).

Figure 5. Hypsometric integral (HI), S_{mf}, and V_f measurements along the Yatağan Fault with respect to different rock strength levels of the geologic units. The dashed black lines represent the L_s segments (S1 and S2). The L_{mf} is identical with the red branch of the Yatağan Fault.

Figure 6. a) 3D view of the topography (generated from 1:25000 scale topographic map) and distribution of channel steepness (θ_{ref} = 0.45) around the Yatağan Fault. Consider the abrupt changes in steepness along mountain front. b) Distribution of channel steepness index with respect to rock strength along the Yatağan Fault.

[4] KOERI-EC (2020). Kandilli Earthquake Catalogue [online]. Website http://www.koeri.boun.edu.tr/sismo/zeqdb/ [accessed 03/2020].

Figure 7. Longitudinal topographic stream profiles of the analyzed catchments along the Yatağan Fault. Red arrows indicate tectonically generated knickpoints along the stream profiles.

Figure 8. Topographic characteristics of the main channel profile of the drainage basin-16. a) Elevation - chi (χ) plot shows relatively transient channel profile. b) Auto k_{sn}- chi (χ) plot shows main variations of steepness along the profile. c) Longitudinal profile of the main channel and its morphologic properties. The profile shows the perfect fit of steepness based on segment definitions. d) Segmentation based on Logarithmic Gradient-Area of the channel and the steepness values.

Figure 9. a) Digital elevation model of the faceted spurs along mountain front of the Yatağan Fault. Blue arrows indicate segment boundaries. White lines show the topographic profiles along the hanging wall and footwall of the Yatağan Fault in Figure 13. Numbers show studied facets. b) View of the faceted spurs along the FS-2 segment of Yatağan Fault (looking to NW).

Figure 10. Results of the hypsometric analysis along footwall of the Yatağan Fault. (a) Distribution of the types of hypsometric curves on DEM. (b) Concave hypsometric curves. (c) S-shaped hypsometric curves. (d) Convex hypsometric curves. (e) Complex hypsometric curves. Db: Drainage basin label.

Figure 11. a) View of drainage basin 4 on DEM, arrows show abrupt anomalies on main stream, b) Longitudinal profile of drainage Db-4, detected tectonic knickpoints indicated with red arrows. c) Photo shows lateral perspective and morphology of the hill which Db-4 lies on it (sight of view is to NW). d) Observed fault scarp during field studies which generate a stair step in morphology and in topographic profile. Fault plane forms a litholologic contact between Mesozoic marble and Miocene clastics (sight of view is to W).

Figure 12. a) View of the footwall block along drainage basins 18 and 19 (sight of view is to W). (b & c) Longitudinal profiles of the drainage basins 18 and 19, detected tectonic knickpoints represented with red arrows. The anomalies generated by rapid uplift along these profiles were identified during field campaigns, it is clear that fault scarp generated by dip-slip motion at mountain front manipulates these streams. The fault plane forms a lithologic contact between Mesozoic marble and recent colluvial deposits.

Figure 13. Topographic profiles of vertical displacement distribution along the Yatağan Fault. Upper profile represents footwall topography (a-a'), while lower-profile represents hanging wall topography (b-b'). Refer to Figure 9 for location of the topographic profiles.

Figure 14. Exponential relationship between vertical slip rate and facet slope. Data compiled from (Tsimi and Ganas, 2015; Topal et al., 2016). AF: Akşehir Fault (Turkey), FS-1 & FS-2: correspond to the Yatağan Fault, NSF: North Sparta Fault (Greece), EF: Elovista Fault (Bulgaria), AtF: Atalanti Fault (Greece), KrF: Krupnik Fault (Bulgaria), GF: Gomati Fault (Greece), SF: Stratoni Fault (Greece), PF: Psathopyrgos Fault (Greece), KaF: Kasteli Fault (Greece), KalF: Kalamata Fault (Greece).

Figure 15 Relationship between plotted S_{mf} and mean V_f values of each segment along the Yatağan Fault on activity classes. Vertical bars indicate standard deviation (σn-1) for V_f values along different fronts. Numbers on the top of the diagram shows inferred uplift rates U (mm/yr) from Rockwell et al. (1985). Red area (class-1) shows uplift rate of ≥ 0.5 mm/yr while yellow part (class-2) show uplift rate between 0.5 and 0.05 mm/yr. Finally, green area (class-3) represents uplift rate of ≤ 0.05.

Table captions

Table 1. Rock strength classification of lithologic units within the study area.

Table 2. Topographic features of the river profiles that were analyzed in this study. Only the knickpoints associated with tectonic perturbation along the river profiles that cross the Yatağan Fault (YF) are considered.

Table 3. Geometric parameters of the triangular facets along the Yatağan Fault extracted from 1:25000 topographic map in ArcGIS 10.3.1. (Elv = Elevation, Min = Minimum, Max = Maximum, m = meter, deg = degree).

Table 4. Values obtained by morphometric indices measurements. Parameters of V_f indice calculated by considering the standard deviation (σn-1) values of each segment.

Supplementary Figure captions

Figure. S1. Topographic characteristics of the main channel profile of the drainage basins 1 and 6. a and e) Elevation - chi (χ) plot of channel profile and transient stage of the profiles. b and f) Auto k_{sn}- chi (χ) plot shows main steepness variations along the profile. c and g) Longitudinal profile of the main channel and its morphologic properties. d and h) Logarithmic slope-area of the channel and steepness based segmentation.

Figure. S2. Topographic characteristics of the main channel profile of the drainage basins 7 and 9. a and e) Elevation - chi (χ) plot of channel profile and transient stage of the profiles. b and f) Auto k_{sn}- chi (χ) plot shows main steepness variations along the profile. c and g) Longitudinal profile of the main channel and its morphologic properties. d and h) Logarithmic Slope-Area of the channel and steepness based segmentation.

Figure. S3. Topographic characteristics of the main channel profile of the drainage basins 12 and 14. a and e) Elevation - chi (χ) plot of channel profile and transient stage of the profiles. b and f) Auto k_{sn}- chi (χ) plot shows main steepness variations along the profile. c and g)

Longitudinal profile of the main channel and its morphologic properties. d and h) Logarithmic slope-area of the

Figure. S4. Topographic characteristics of the main channel profile of the drainage basins 16 and 21. a and e) Elevation - chi (χ) plot of channel profile and transient stage of the profiles. b and f) Auto k_{sn}- chi (χ) plot shows main steepness variations along the profile. c and g) Longitudinal profile of the main channel and its morphologic properties. d and h) Logarithmic slope-area of the channel and steepness based segmentation.

Figure. S5. (a) Projected tilt corrected paleomagnetic inclination values of the SW Anatolia Domain (inclination degrees and station data compiled from Kaymakcı et al., 2018). Small black dots (P) indicate studied sites; besides, contour lines show calculated inclination angles in degree mainly in Neogene period (please review Kaymakcı et al., 2018 for more information regarding the paleomagnetic investigations). Each contour line depicts 0.5 interval of tilt corrected inclination variation. Solid black line represents the location of cross section that virtually run through the orientation of the Yatağan Fault. (b) cross section indicates the variation of inclination degree along with distance from the north west towards the south eastern margin of the basin.

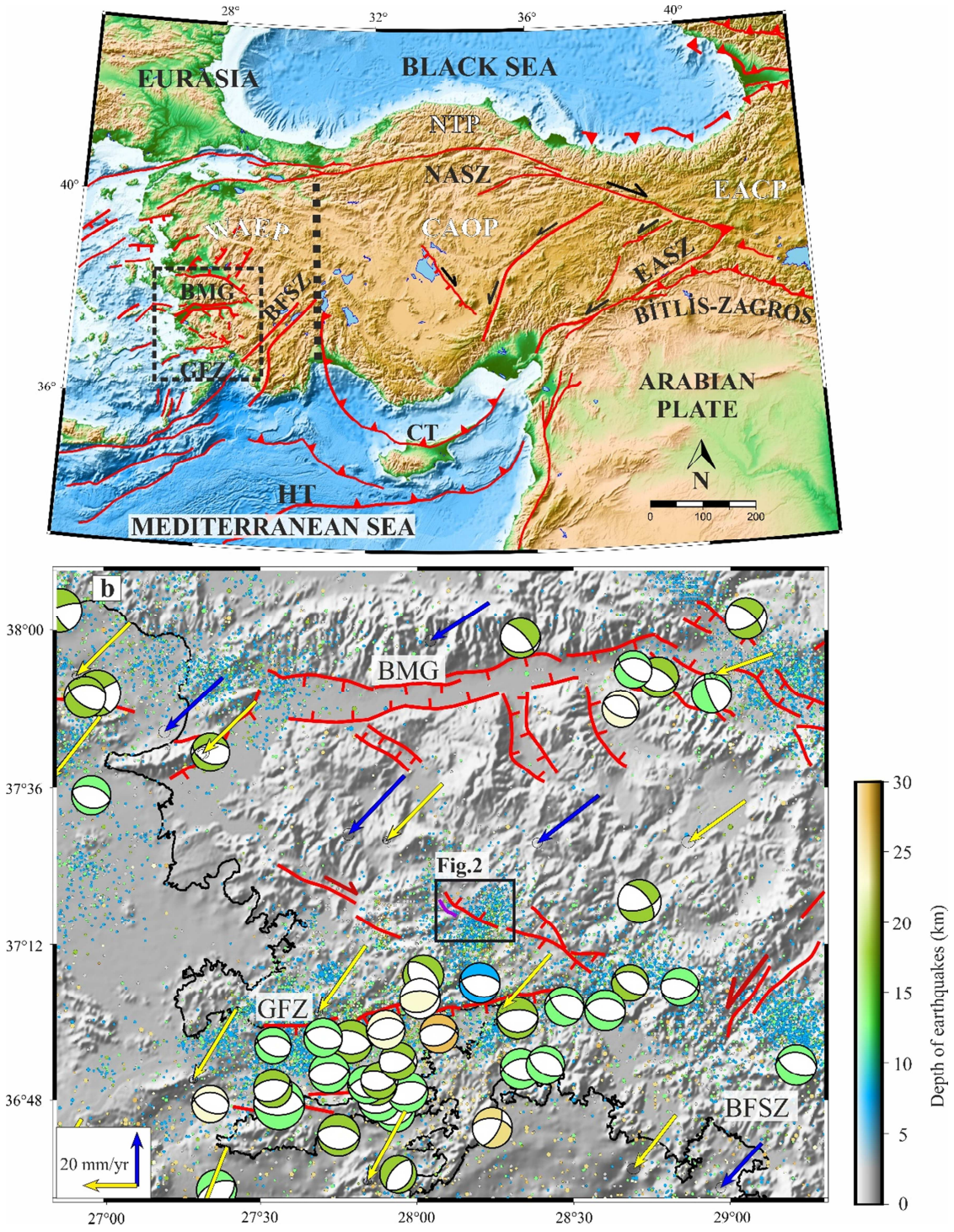

Figure 1. a) Simplified neotectonic setting of the Turkey and surrounding area. Dashed line represents the proposed boundary between WAEP and CAOP (Şengör et al., 1985; 2014; Emre

et al., 2013; Hall et al., 2014; Şengör and Zabcı, 2019). EACP: Eastern Anatolia Compressional Province, CAOP: Central Anatolia Ova Province, NTP: North Turkish Province, WAEP: Western Anatolia Extensional Province, NAFZ: North Anatolian Fault Zone, EAFZ: Eastern Anatolian Fault Zone, HT: Hellenic Trench, BMG: Büyük Menderes Graben, GFZ: Gökova Fault Zone, BFSZ: Burdur-Fethiye Shear Zone, CT: Cyprus Trench, MF: Muğla Fault. The dashed rectangular shows the location of the study area in Figure 1b. Topographic and bathymetric base maps are available at GEBCO data and products (GEBCO-GBD, 2019[5]). b) Seismotectonic map of the SW Turkey (faults from Emre et al., 2013). Small circles indicate seismic activity ($M_w \geq 2.5$) and are colored depending on their hypocenter depth between 1900 and 2020 (KOERI-EC, 2020[6]). Yellow and blue arrows indicate counterclockwise rotation relative to Eurasia (yellow and blue arrows are adopted from Reilinger et al., 2006 and England et al., 2016 respectively). Focal mechanisms of earthquakes that occurred during instrumental period (1965-2020) were compiled from Kiratzi and Louvari (2003) and CMT Harvard catalogue (2020)[7].

[5] GEBCO-GBD (2019). Gridded Bathymetry Data [online]. Website http://www.gebco.net /data_and_products/gridded_batymetry_data/ [accessed 11/2019].

[6] KOERI-EC (2020). Kandilli Earthquake Catalogue [online]. Website http://www.koeri. boun.edu.tr/sismo/zeqdb/ [accessed 03/2020].

[7] Global CMT Catalogue (2020). Global CMT Catalog Search [online]. Website https:// www.globalcmt.org/CMTsearch.html [accessed 03/2020].

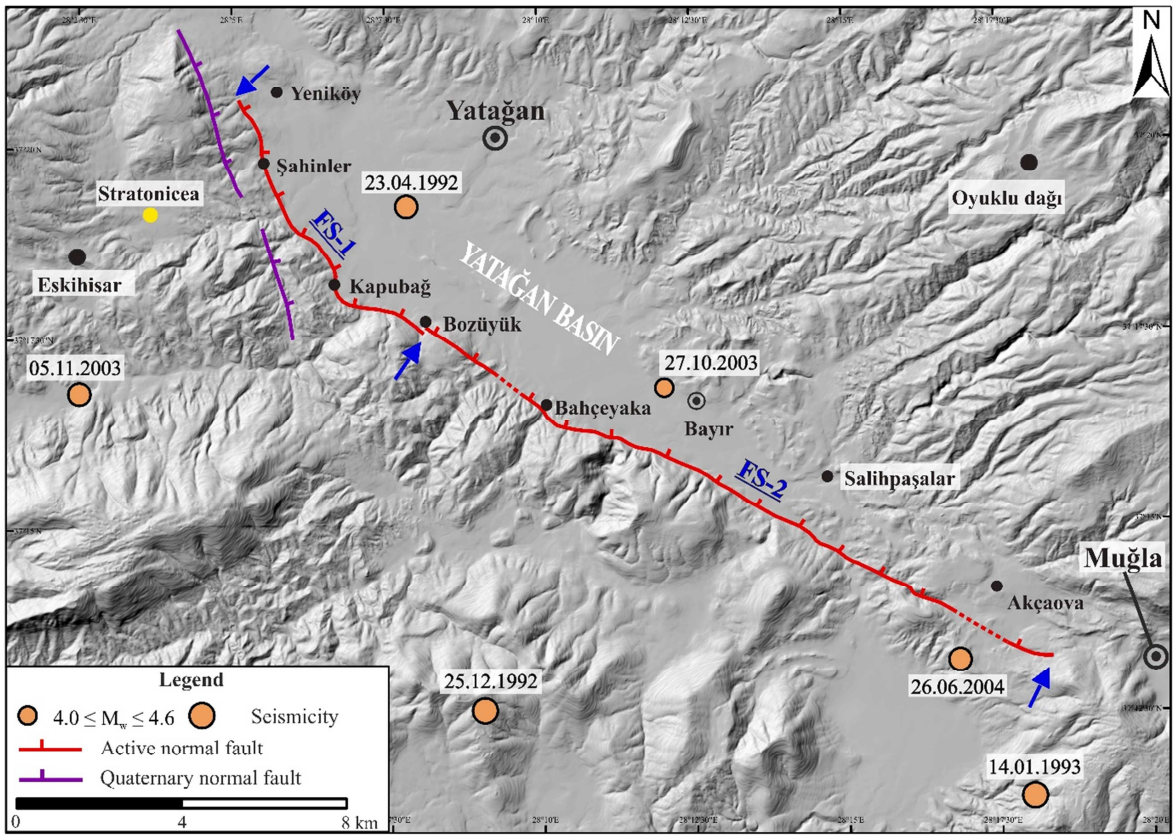

Figure. 2 Seismotectonic map of the Yatağan Fault. Quaternary and active faults are compiled and simplified from Emre et al. (2013) and Basmenji et al. (2020). Blue arrows indicate the segment boundaries. Black circles show location of the modern cities and villages. The earthquake data is from KOERI-EC (2020[8]).

[8] KOERI-EC (2020). Kandilli Earthquake Catalogue [online]. Website http://www.koeri.boun.edu.tr/sismo/zeqdb/ [accessed 03/2020].

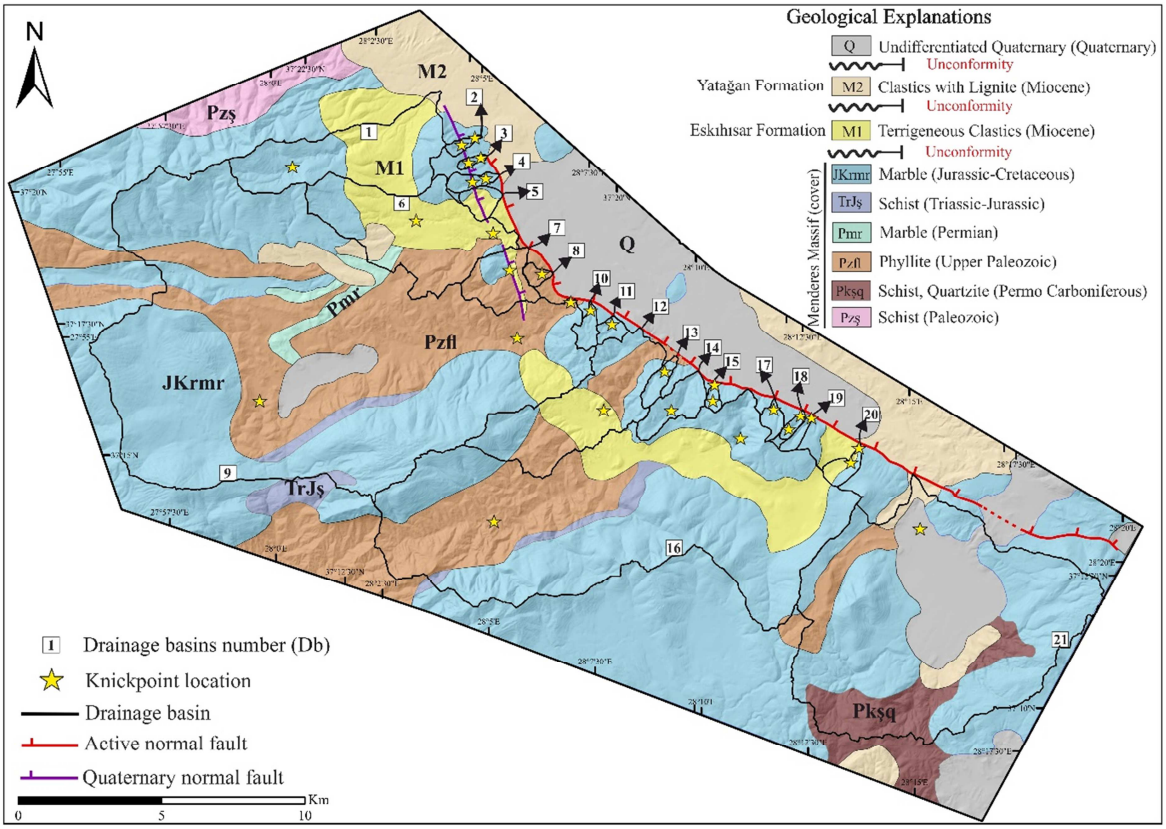

Figure 3. Simplified geologic map of the study area (compiled from Atalay, 1980; Akbaş et al., 2011; Gürer et al., 2013).

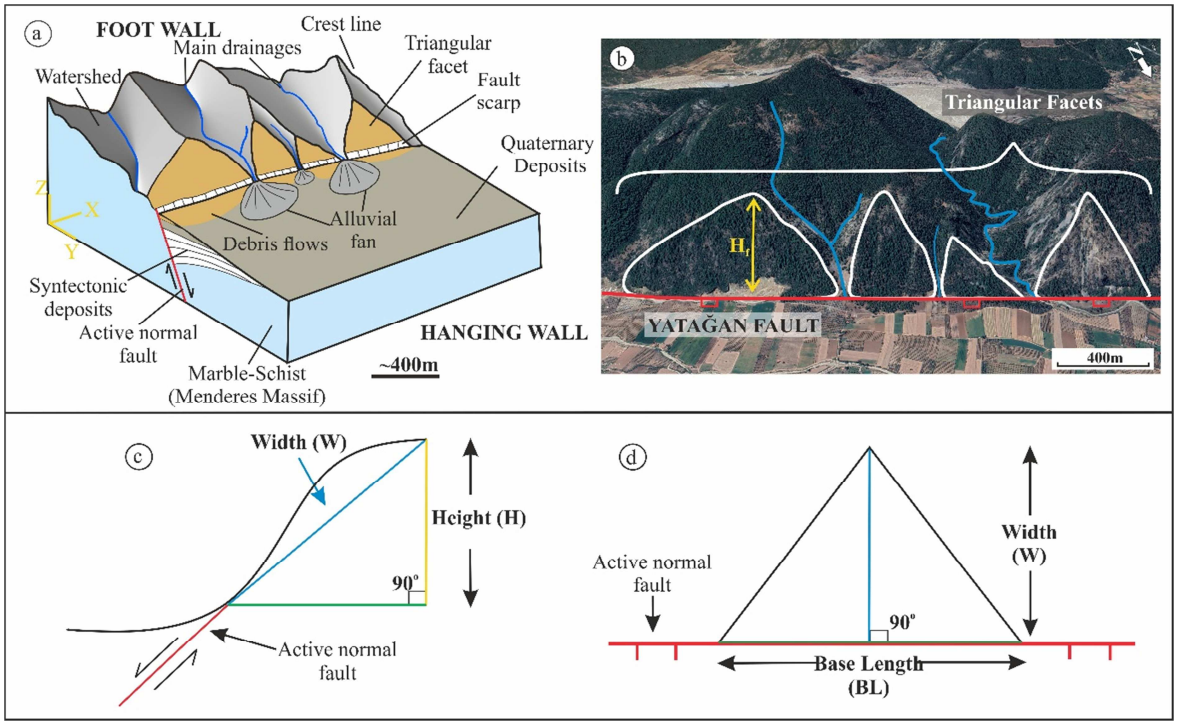

Figure 4. a) Simplified block diagram represents structural framework of a normal fault and related morphologic characteristics (inspired and modified after Wallace, 1978; Strak et al., 2011). b) Google Earth view of the faceted spurs along the Yatağan Fault and associated morphologic characteristics, H_f is the triangular facet basal height. c) Graphic shows the cross-section view of a triangular facet, Width: represent distance from top of facet to base, Height: is defined as the difference between maximum elevation and base elevation. d) Front aspect of a triangular facet on footwall of a normal fault. c & d adapted and modified after Tsimi and Ganas (2015).

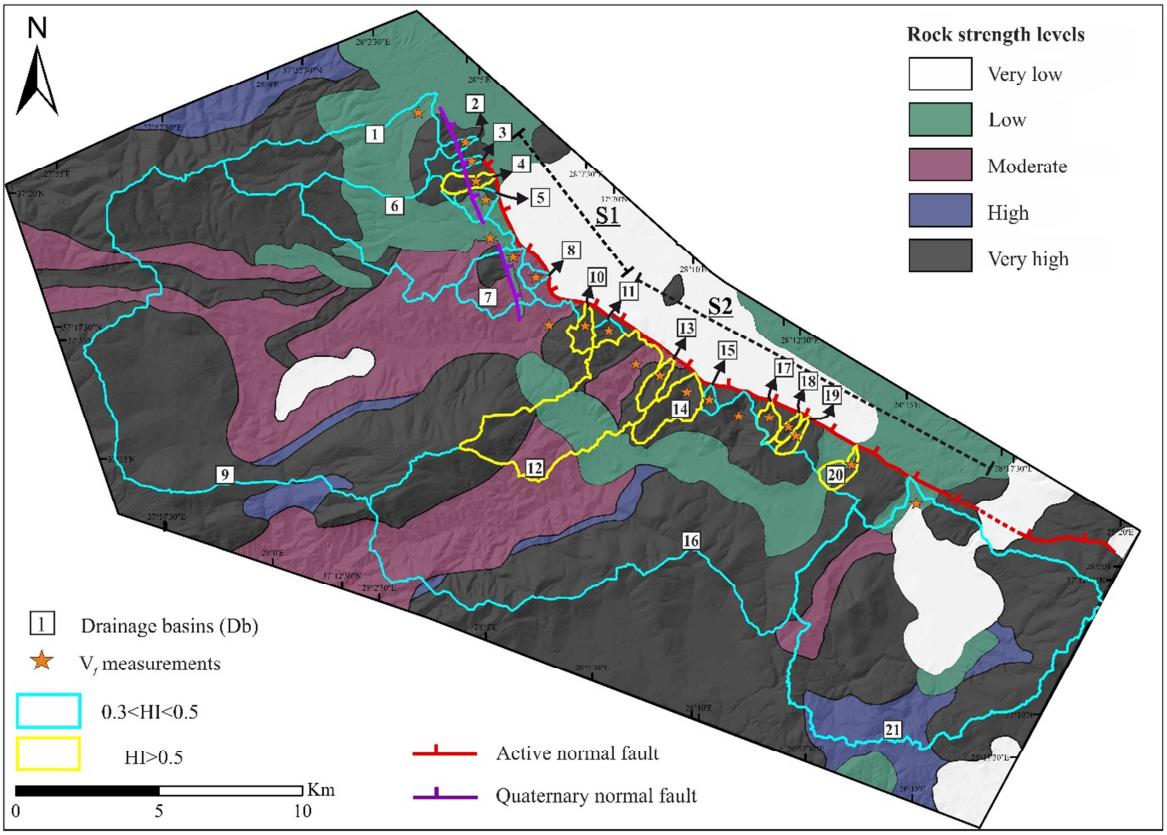

Figure 5. Hypsometric integral (HI), S_{mf}, and V_f measurements along the Yatağan Fault with respect to different rock strength levels of the geologic units. The dashed black lines represent the L_s segments (S1 and S2). The L_{mf} is identical with the red branch of the Yatağan Fault.

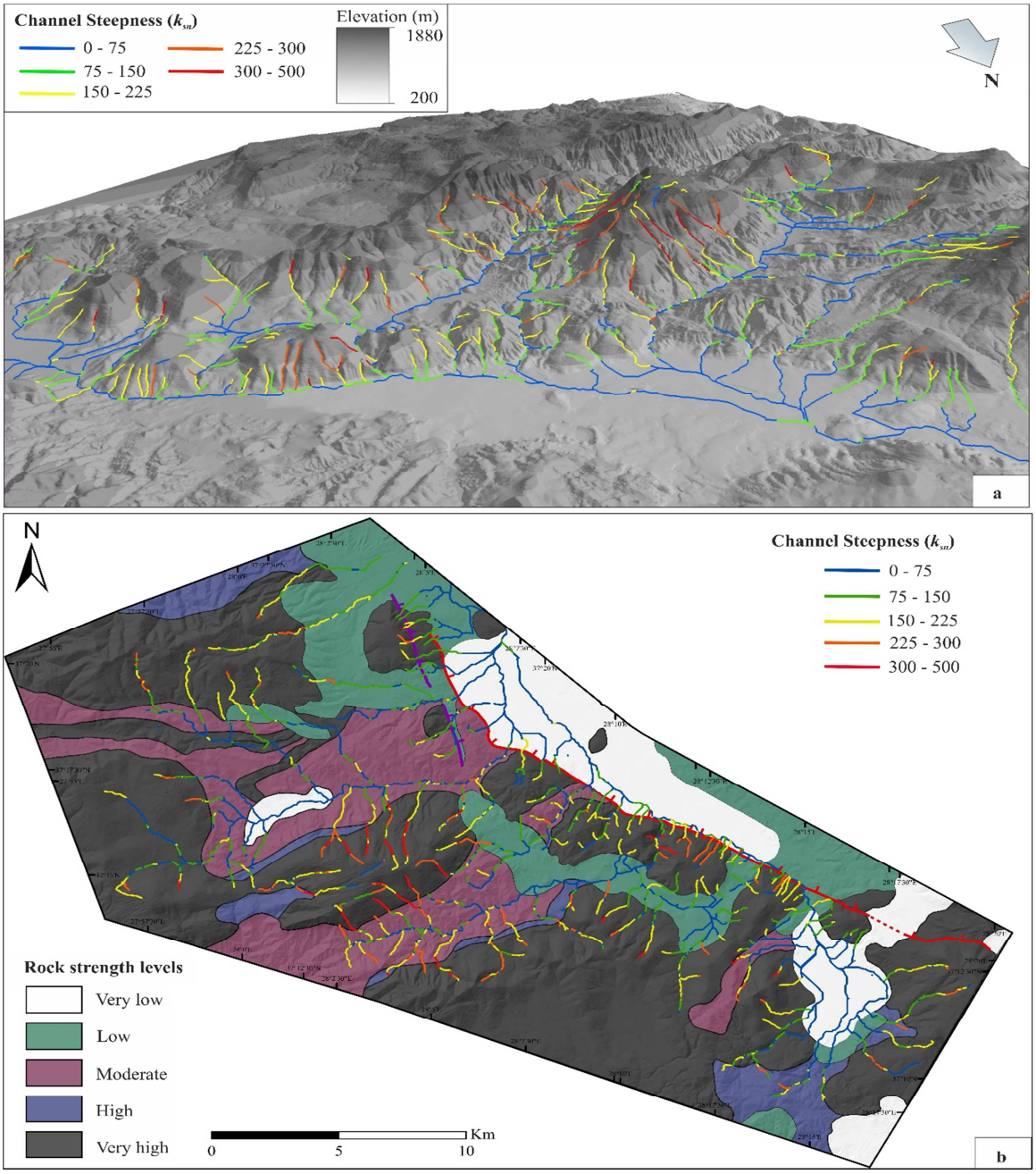

Figure 6. a) 3D view of the topography (generated from 1:25000 scale topographic map) and distribution of channel steepness (θ_{ref} = 0.45) around the Yatağan Fault. Consider the abrupt changes in steepness along mountain front. b) Distribution of channel steepness index with respect to rock strength along the Yatağan Fault.

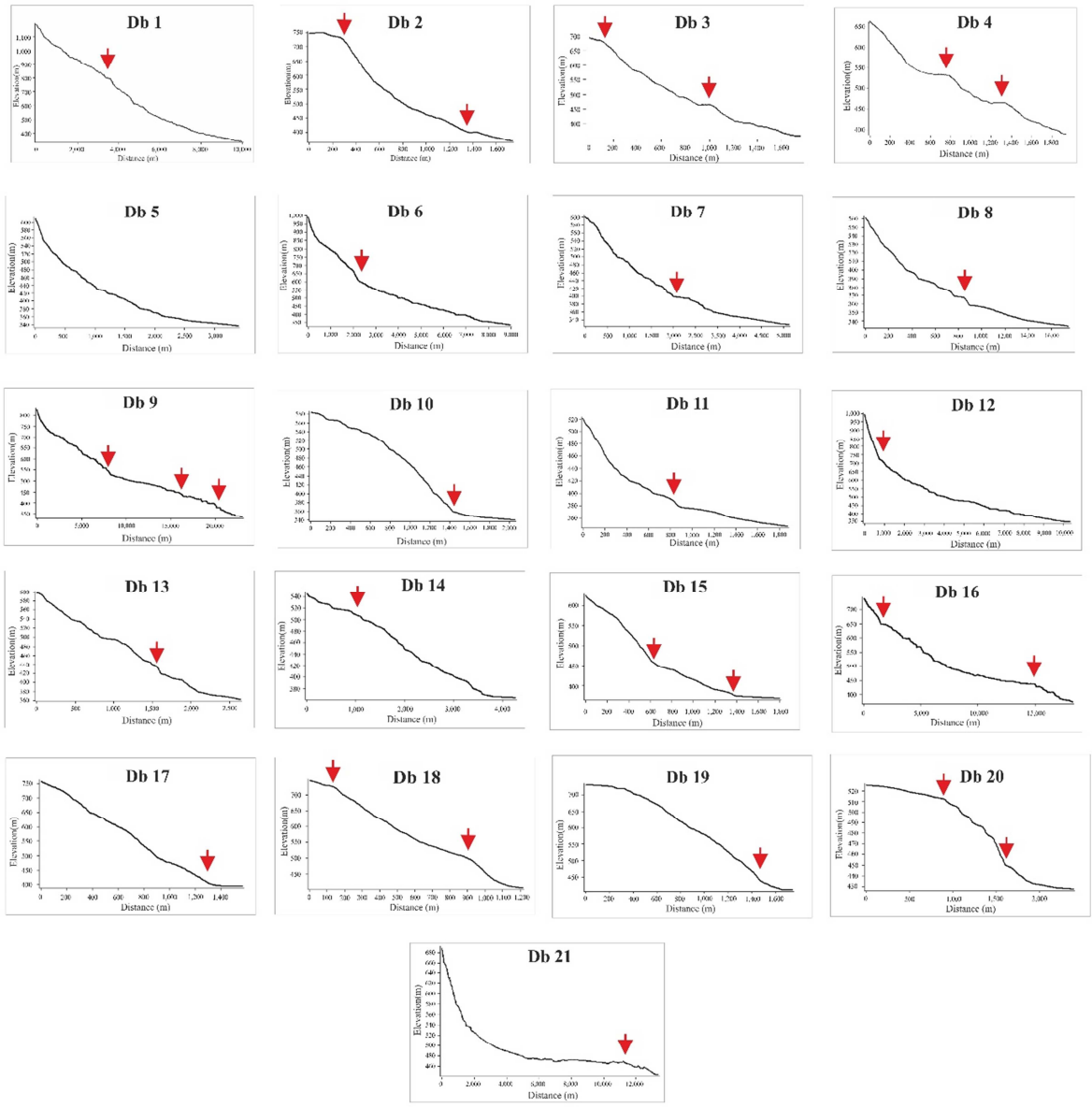

Figure 7. Longitudinal topographic stream profiles of the analyzed catchments along the Yatağan Fault. Red arrows indicate tectonically generated knickpoints along the stream profiles.

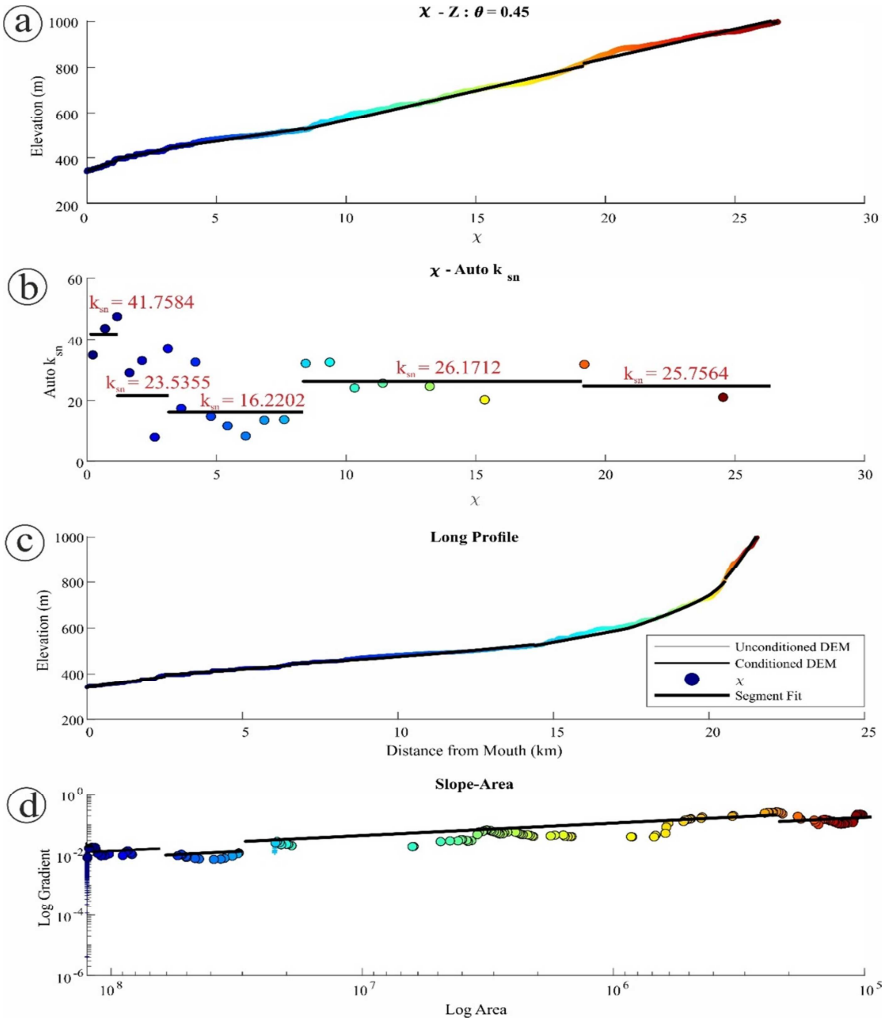

Figure 8. Topographic characteristics of the main channel profile of the drainage basin-16. a) Elevation - chi (χ) plot shows relatively transient channel profile. b) Auto k_{sn}- chi (χ) plot shows main variations of steepness along the profile. c) Longitudinal profile of the main channel and its morphologic properties. The profile shows the perfect fit of steepness based on segment definitions. d) Segmentation based on Logarithmic Gradient-Area of the channel and the steepness values.

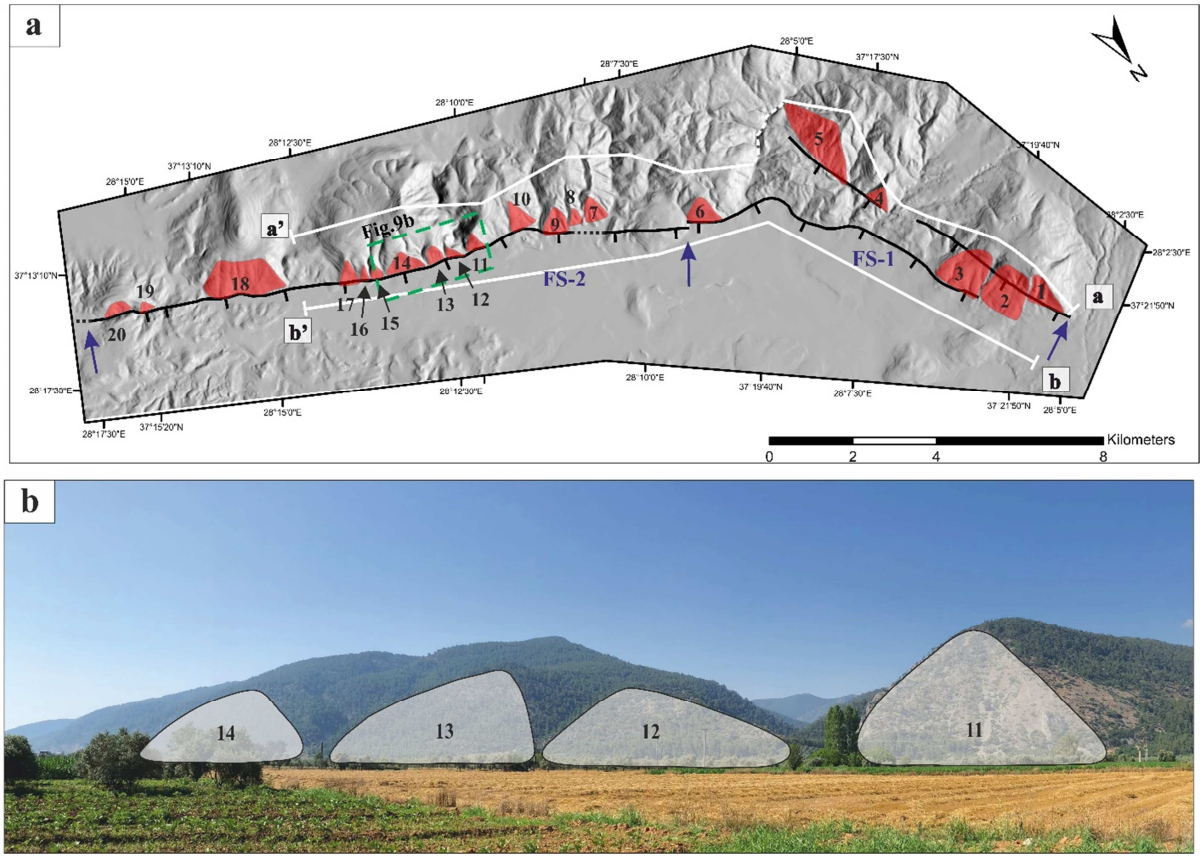

Figure 9. a) Digital elevation model of the faceted spurs along mountain front of the Yatağan Fault. Blue arrows indicate segment boundaries. White lines show the topographic profiles along the hanging wall and footwall of the Yatağan Fault in Figure 13. Numbers show studied facets. b) View of the faceted spurs along the FS-2 segment of Yatağan Fault (looking to NW).

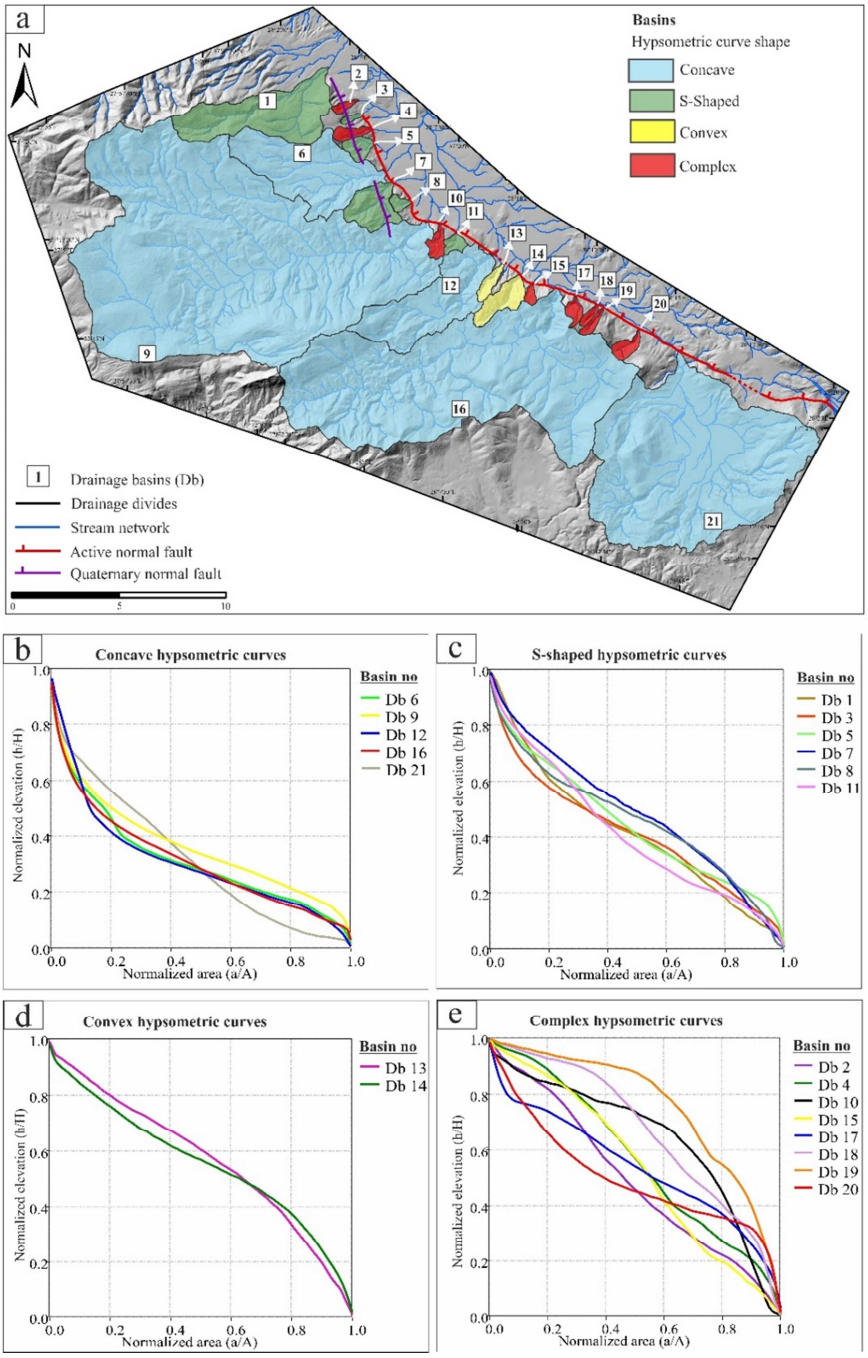

Figure 10. Results of the hypsometric analysis along footwall of the Yatağan Fault. (a) Distribution of the types of hypsometric curves on DEM. (b) Concave hypsometric curves. (c) S-shaped hypsometric curves. (d) Convex hypsometric curves. (e) Complex hypsometric curves. Db: Drainage basin label.

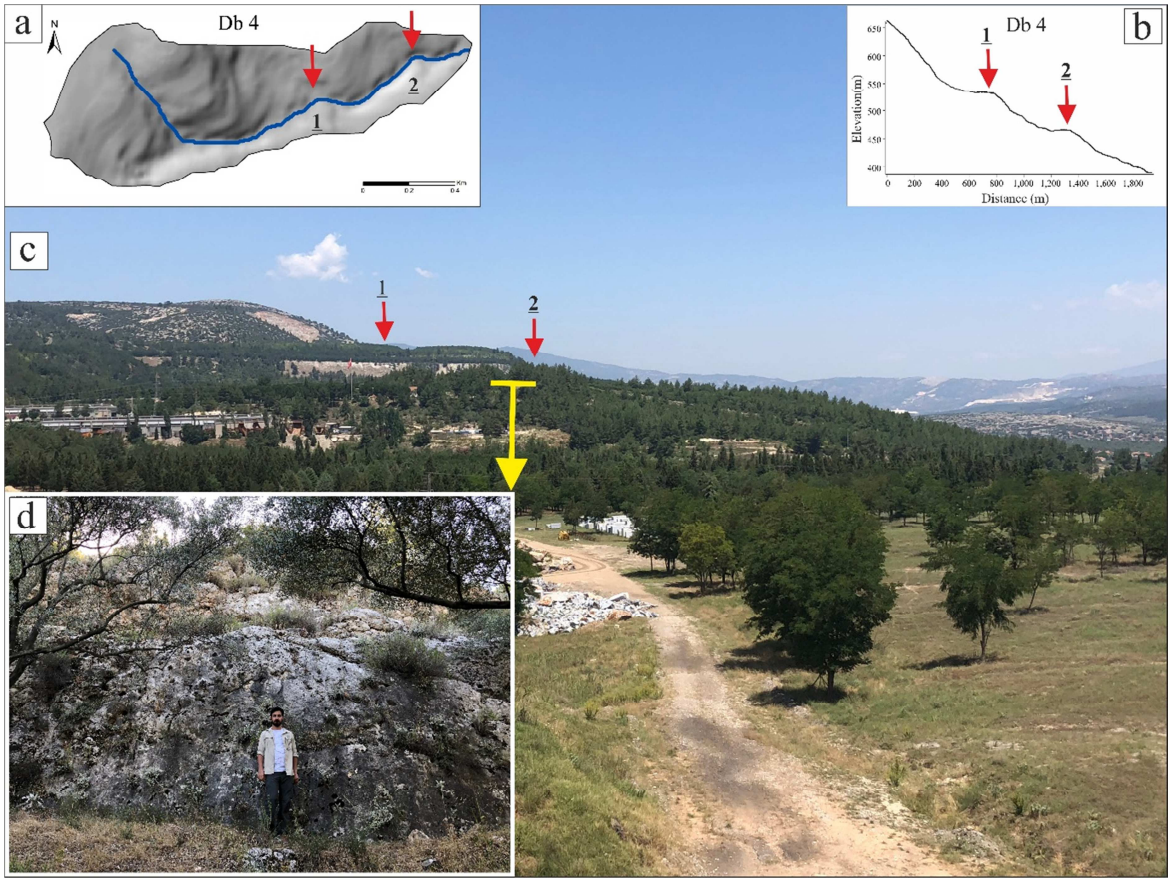

Figure 11. a) View of drainage basin 4 on DEM, arrows show abrupt anomalies on main stream, b) Longitudinal profile of drainage Db-4, detected tectonic knickpoints indicated with red arrows. c) Photo shows lateral perspective and morphology of the hill which Db-4 lies on it (sight of view is to NW). d) Observed fault scarp during field studies which generate a stair step in morphology and in topographic profile. Fault plane forms a litholologic contact between Mesozoic marble and Miocene clastics (sight of view is to W).

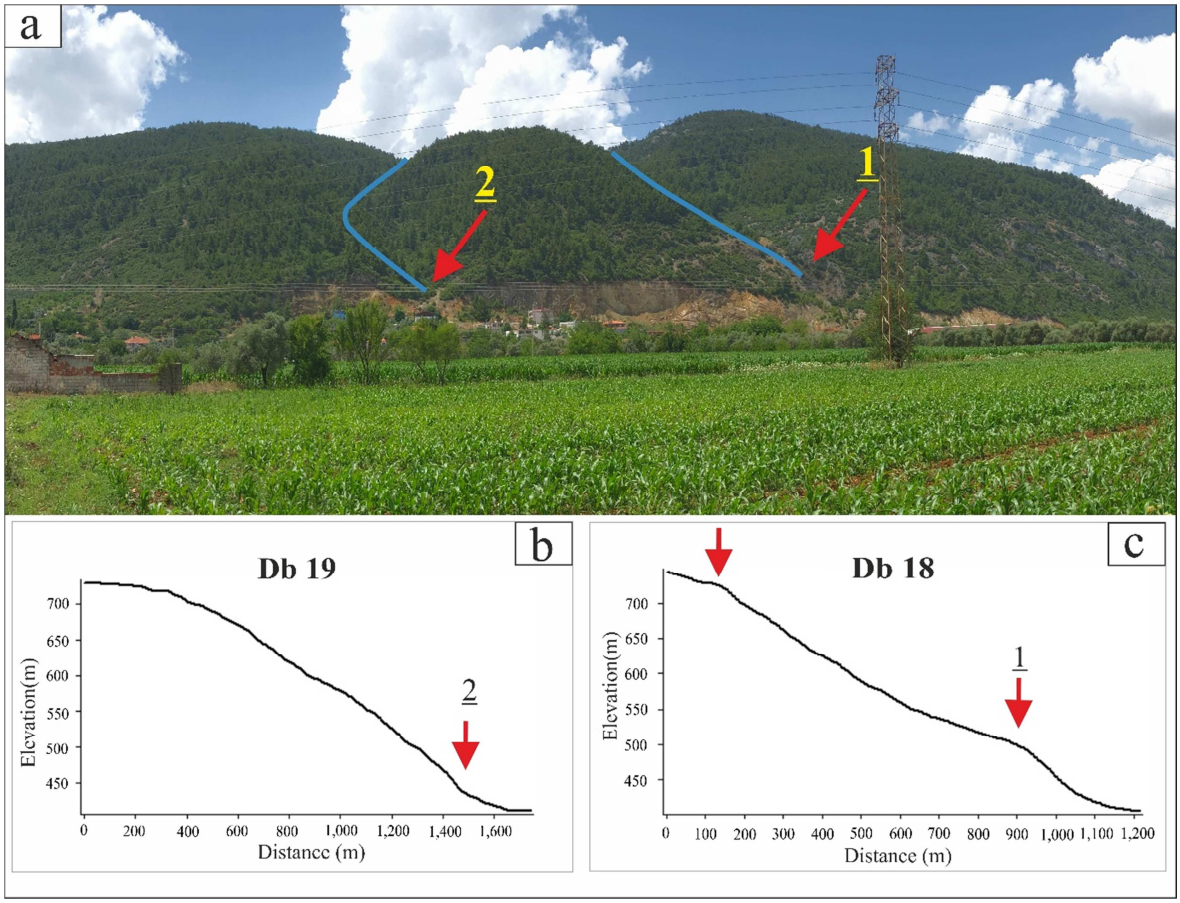

Figure 12. a) View of the footwall block along drainage basins 18 and 19 (sight of view is to W). (b & c) Longitudinal profiles of the drainage basins 18 and 19, detected tectonic knickpoints represented with red arrows. The anomalies generated by rapid uplift along these profiles were identified during field campaigns, it is clear that fault scarp generated by dip-slip motion at mountain front manipulates these streams. The fault plane forms a lithologic contact between Mesozoic marble and recent colluvial deposits.

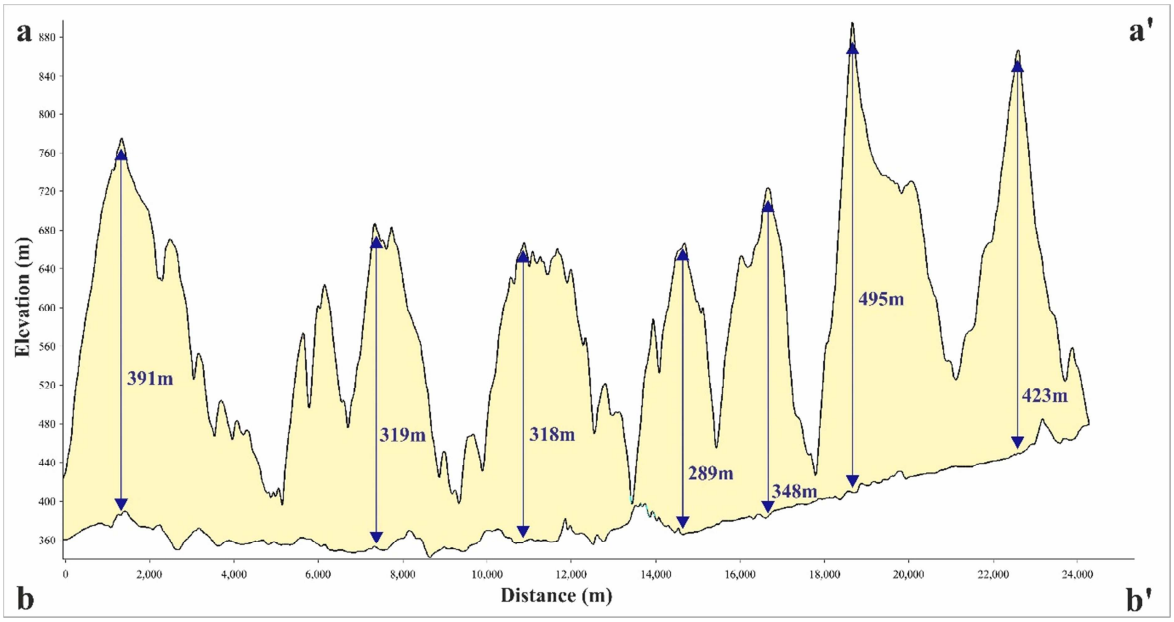

Figure 13. Topographic profiles of vertical displacement distribution along the Yatağan Fault. Upper profile represents footwall topography (a-a'), while lower-profile represents hanging wall topography (b-b'). Refer to Figure 9 for location of the topographic profiles.

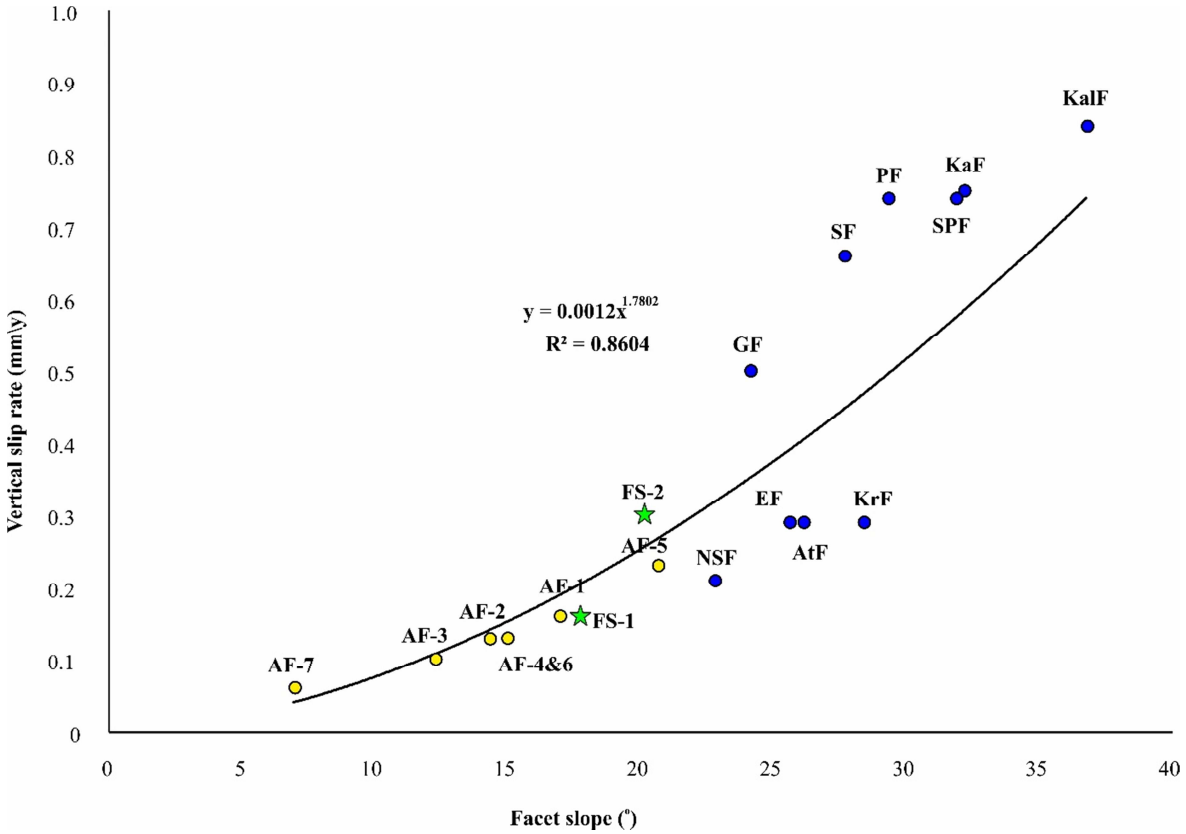

Figure 14. Exponential relationship between vertical slip rate and facet slope. Data compiled from (Tsimi and Ganas, 2015; Topal et al., 2016). AF: Akşehir Fault (Turkey), FS-1 & FS-2: correspond to the Yatağan Fault, NSF: North Sparta Fault (Greece), EF: Elovista Fault (Bulgaria), AtF: Atalanti Fault (Greece), KrF: Krupnik Fault (Bulgaria), GF: Gomati Fault (Greece), SF: Stratoni Fault (Greece), PF: Psathopyrgos Fault (Greece), KaF: Kasteli Fault (Greece), KalF: Kalamata Fault (Greece).

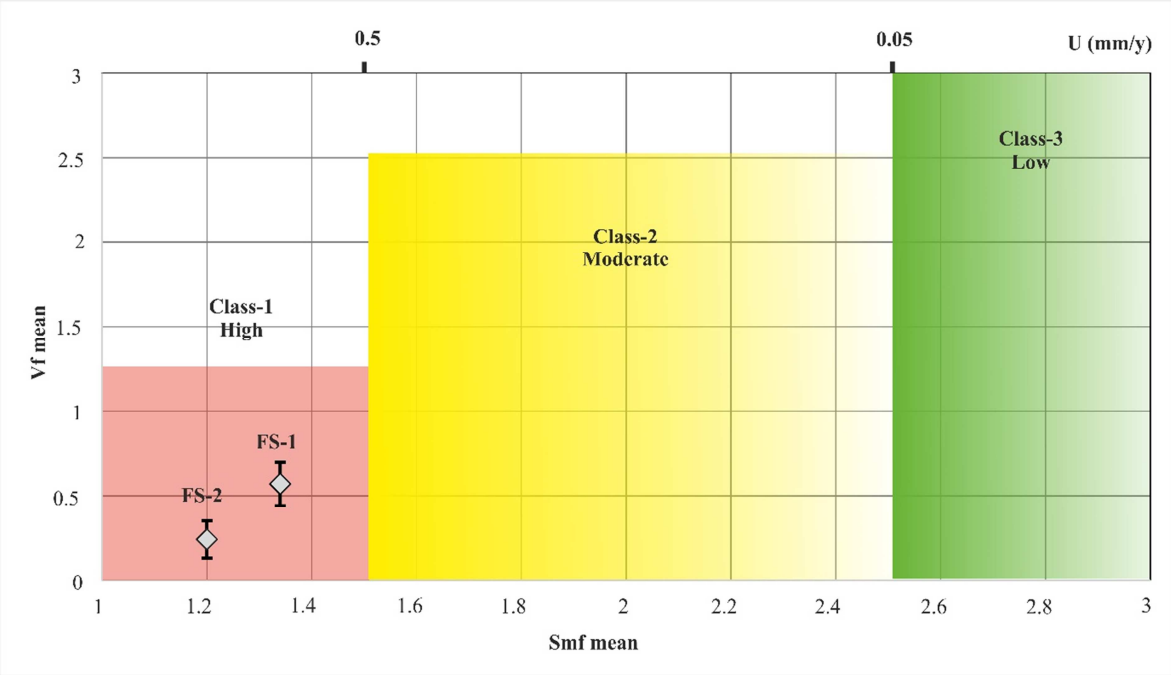

Figure 15. Relationship between plotted S_{mf} and mean V_f values of each segment along the Yatağan Fault on activity classes. Vertical bars indicate standard deviation (σn-1) for V_f values along different fronts. Numbers on the top of the diagram shows inferred uplift rates U (mm/yr) from Rockwell et al. (1985). Red area (class-1) shows uplift rate of ≥ 0.5 mm/yr while yellow part (class-2) show uplift rate between 0.5 and 0.05 mm/yr. Finally, green area (class-3) represents uplift rate of ≤ 0.05.

Table 1. Rock strength classification of lithologic units within the study area.

Rock characteristic	Schmidt Hammer type		Description [b]
	N - type 'R'[a]	L - type 'R'	
Weakly compacted and poorly sorted Quaternary Deposits - alluvium, debris flows, colluvial and fluvial deposits	–	–	Very low rock strength - crumbles under sharp blows with geological pick point, can be cut with pocket knife
Weakly cemented sedimentary deposits - lacustrine sediments and older fluvial deposits containing poorly consolidate clastics	–	–	Weak rock strength - shallow cuts or scraping with pocket knife, pick points indents deeply with firm blow
Metamorphic rocks - phyllite	23 - 32	31.1 – 38.4	Moderate rock strength - scraping with pocket knife with difficulty, deep indentation under firm blow from pick point
Metamorphic rocks - schist	26.6 – 42.7	29.2 – 30.9	High rock strength - pocket knife cannot use to peel or scrape surface, shallow indentation under firm blow form pick point
Competent metamorphic rock -	58 - 62	50 - 52	Very high rock strength - breaks

marble			with one or more firm blow from hammer end of the geological pick

[a] R represents rebound value of metamorphic rocks after the application of the N and L type Schmidt Hammers (Özbek et al., 2018).

[b] descriptions modified after Selby (1980) and Goudie (2006).

Table 2. Topographic features of the river profiles that were analyzed in this study. Only the knickpoints associated with tectonic perturbation along the river profiles that cross the Yatağan Fault (YF) are considered.

Channel No	Channel Length (km)	Catchment Area (km^2)	Knickpoint elevation (m)	K_{sn} upstream of Knickpoint	K_{sn} downstream of Knickpoint	YF elevation (m)	Distance to active fault (m)
1	9.8	14.2	898	104.02	229.51	419	4285
6	10.3	16.5	518	93.46	110.72	355	3923
			427	110.72	179.01	355	1222
7	4.4	4.0	568	50.03	72.16	362	2497
9	22.4	124.6	516	25.75	26.17	354	12416
			444	16.22	23.53	354	5925
			397	23.53	41.75	354	2340
12	11.6	14.9	459	951.86	998.48	368	3445
14	4.3	2.6	495	23.42	67.99	387	1916
16	19.9	78.3	436	75.53	95.78	444	1837
			598	38.92	172.65	444	11929
21	12.3	64.5	466	8.02	78.73	459	2129

Table 3. Geometric parameters of the triangular facets along the Yatağan Fault extracted from 1:25000 topographic map in ArcGIS 10.3.1. (Elv = Elevation, Min = Minimum, Max = Maximum, m = meter, deg = degree).

Facet No	Max Elv (m)	Min Elv (m)	Min Elv - Max Elv (m)	Horizontal distance (m)	Slope angle (deg)
1	695	555	140	315	23.96
2	490	398	92	415	12.49
3	464	404	60	280	12.09
4	500	375	125	315	21.64
5	540	360	180	510	19.44
6	580	450	130	430	16.82
7	525	370	155	490	17.55
8	510	406	104	400	14.57
9	560	385	175	640	15.29
10	486	400	86	375	12.91
11	494	398	96	410	13.17
12	637	460	177	645	15.34
13	545	400	145	295	26.17
14	675	390	285	455	32.06
15	595	415	180	335	28.24
16	655	410	245	465	27.78
17	605	420	185	360	27.19

18	680	460	220	837	14.72
19	605	435	170	423	21.89
20	650	435	215	580	20.33

Table 4. Values obtained by morphometric indices measurements. Parameters of V_f indice calculated by considering the standard deviation (σn-1) values of each segment.

Catchement No	segment	HI	Segment Length (km)	Mean S_{mf}	V_f			
					n	V_f	mean	σn-1
1	FS-1	0.411	10.5	1.34	3	0.92	0.64	0.11
2	FS-1	0.497			3	1.03		
3	FS-1	0.418			3	0.50		
4	FS-1	0.572			3	0.53		
5	FS-1	0.414			3	2.07		
6	FS-1	0.318			3	0.37		
7	FS-1	0.444			3	0.21		
8	FS-1	0.487			3	0.40		
9	FS-1	0.366			3	0.22		
10	FS-1	0.646			3	0.21		
11	FS-1	0.460	19.5	1.2	3	0.22	0.24	0.09
12	FS-2	0.310			3	0.21		
13	FS-2	0.573			3	0.28		
14	FS-2	0.559			3	0.17		
15	FS-2	0.539			3	0.30		
16	FS-2	0.315			3	0.07		
17	FS-2	0.541			3	0.30		
18	FS-2	0.670			3	0.24		

19	FS-2	0.761			3	0.25		
20	FS-2	0.507			3	0.23		
21	FS-2	0.322			3	0.39		

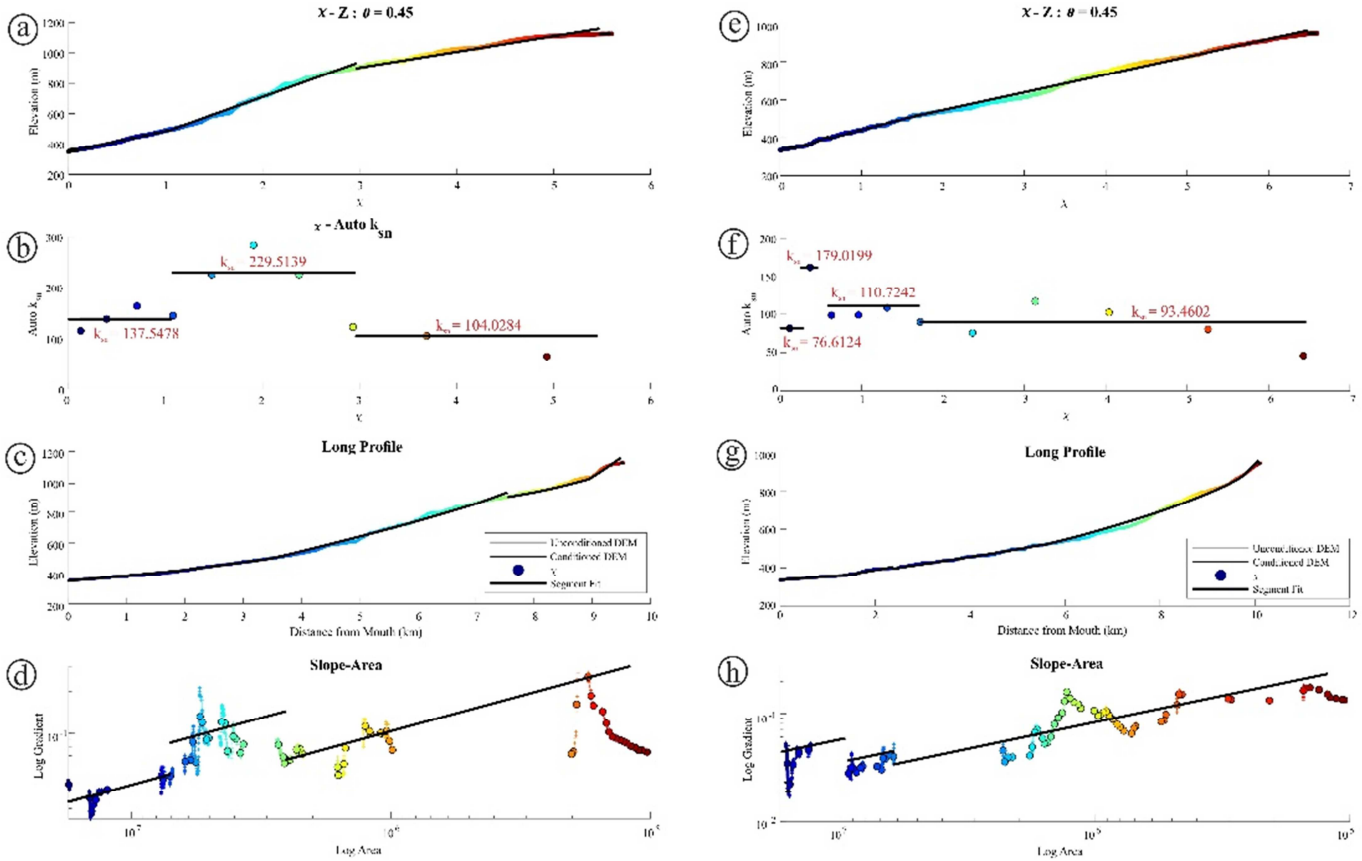

Figure. S1. Topographic characteristics of the main channel profile of the drainage basins 1 and 6. a and e) Elevation - chi (χ) plot of channel profile and transient stage of the profiles. b and f) Auto k_{sn}- chi (χ) plot shows main steepness variations along the profile. c and g) Longitudinal profile of the main channel and its morphologic properties. d and h) Logarithmic slope-area of the channel and steepness based segmentation.

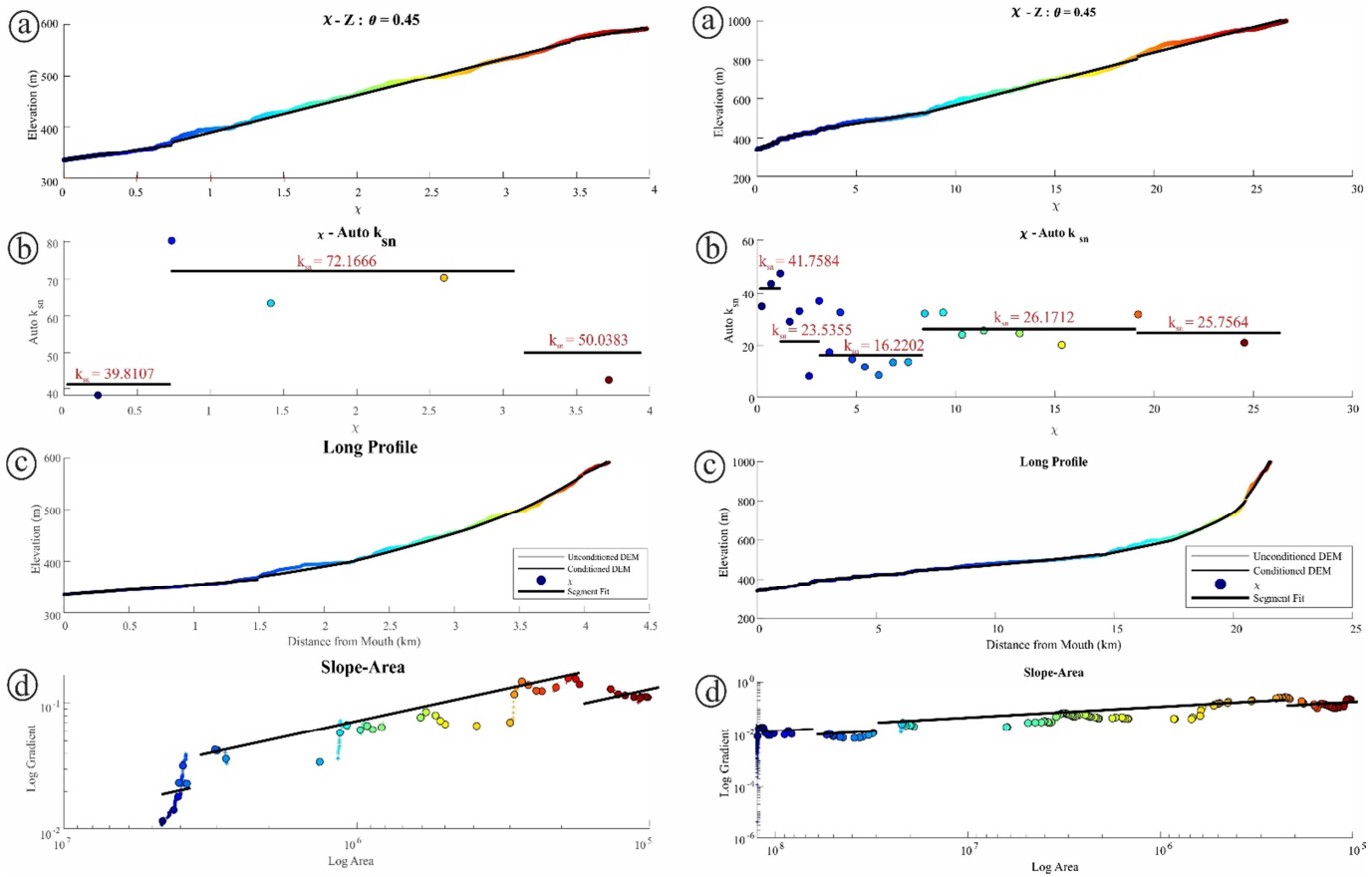

Figure. S2. Topographic characteristics of the main channel profile of the drainage basins 7 and 9. a and e) Elevation - chi (χ) plot of channel profile and transient stage of the profiles. b and f) Auto k_{sn}- chi (χ) plot shows main steepness variations along the profile. c and g) Longitudinal profile of the main channel and its morphologic properties. d and h) Logarithmic Slope-Area of the channel and steepness based segmentation.

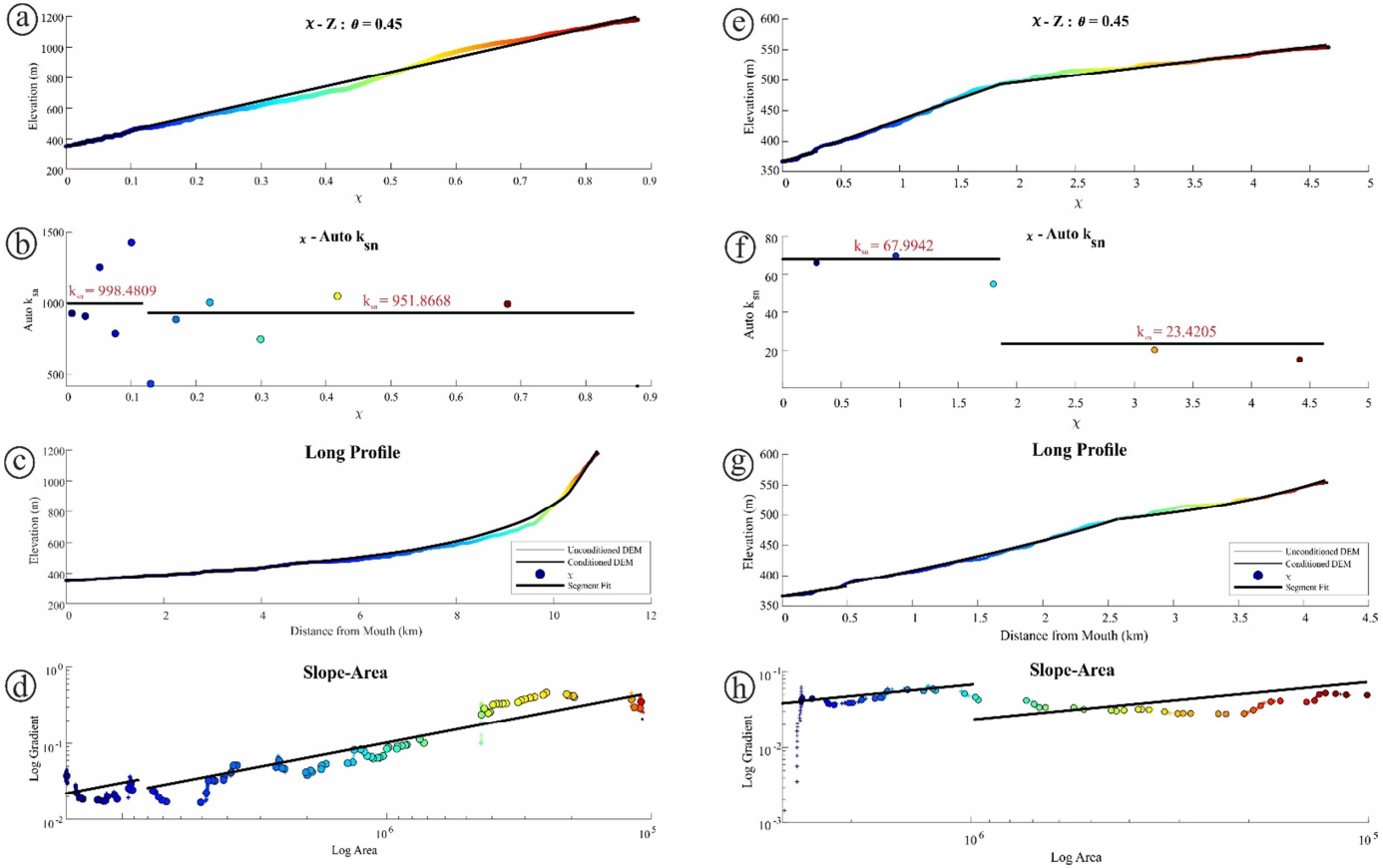

Figure. S3. Topographic characteristics of the main channel profile of the drainage basins 12 and 14. a and e) Elevation - chi (χ) plot of channel profile and transient stage of the profiles. b and f) Auto k_{sn}- chi (χ) plot shows main steepness variations along the profile. c and g) Longitudinal profile of the main channel and its morphologic properties. d and h) Logarithmic slope-area of the channel and steepness based segmentation.

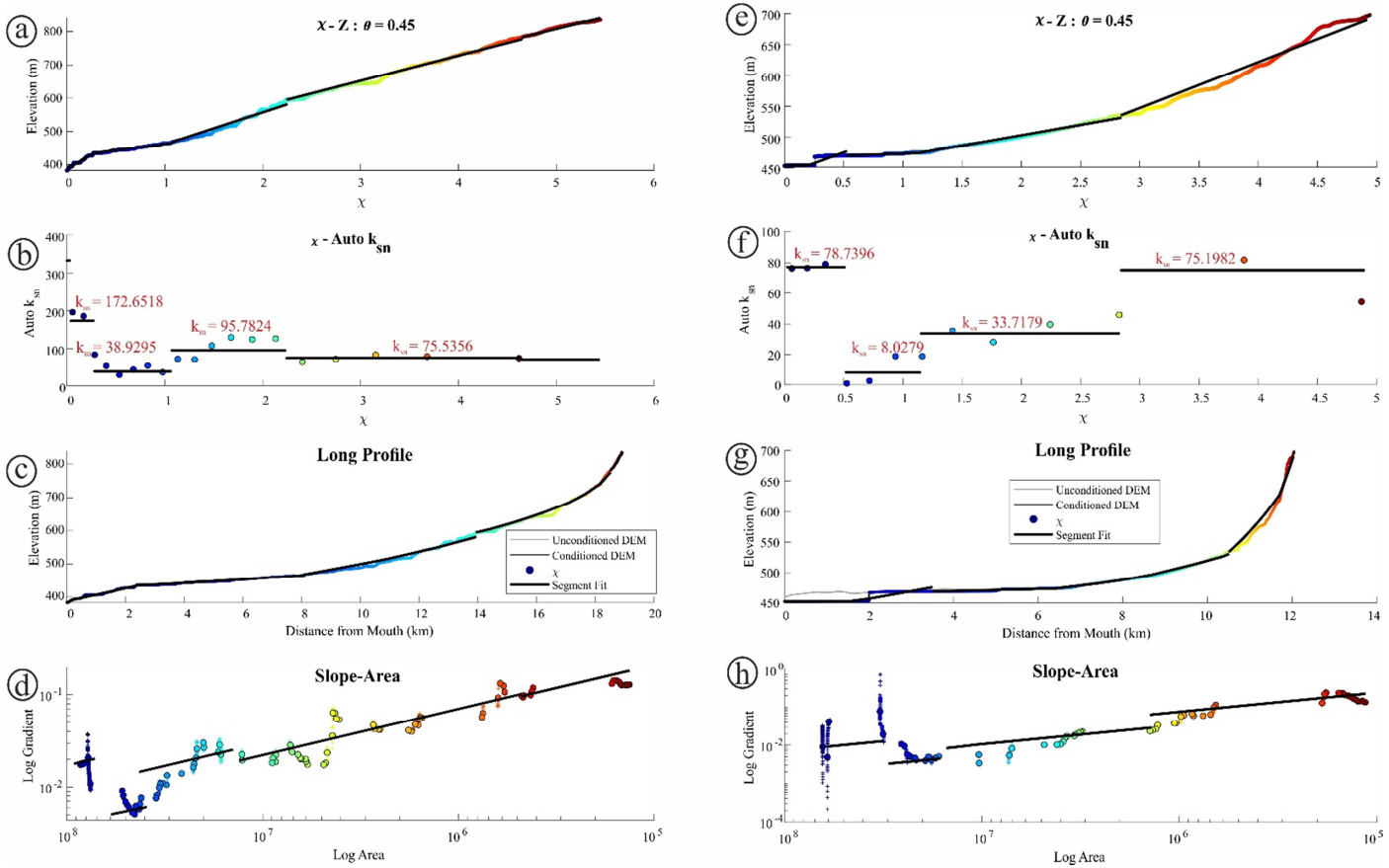

Figure. S4. Topographic characteristics of the main channel profile of the drainage basins 16 and 21. a and e) Elevation - chi (χ) plot of channel profile and transient stage of the profiles. b and f) Auto k_{sn}- chi (χ) plot shows main steepness variations along the profile. c and g) Longitudinal profile of the main channel and its morphologic properties. d and h) Logarithmic slope-area of the channel and steepness based segmentation.

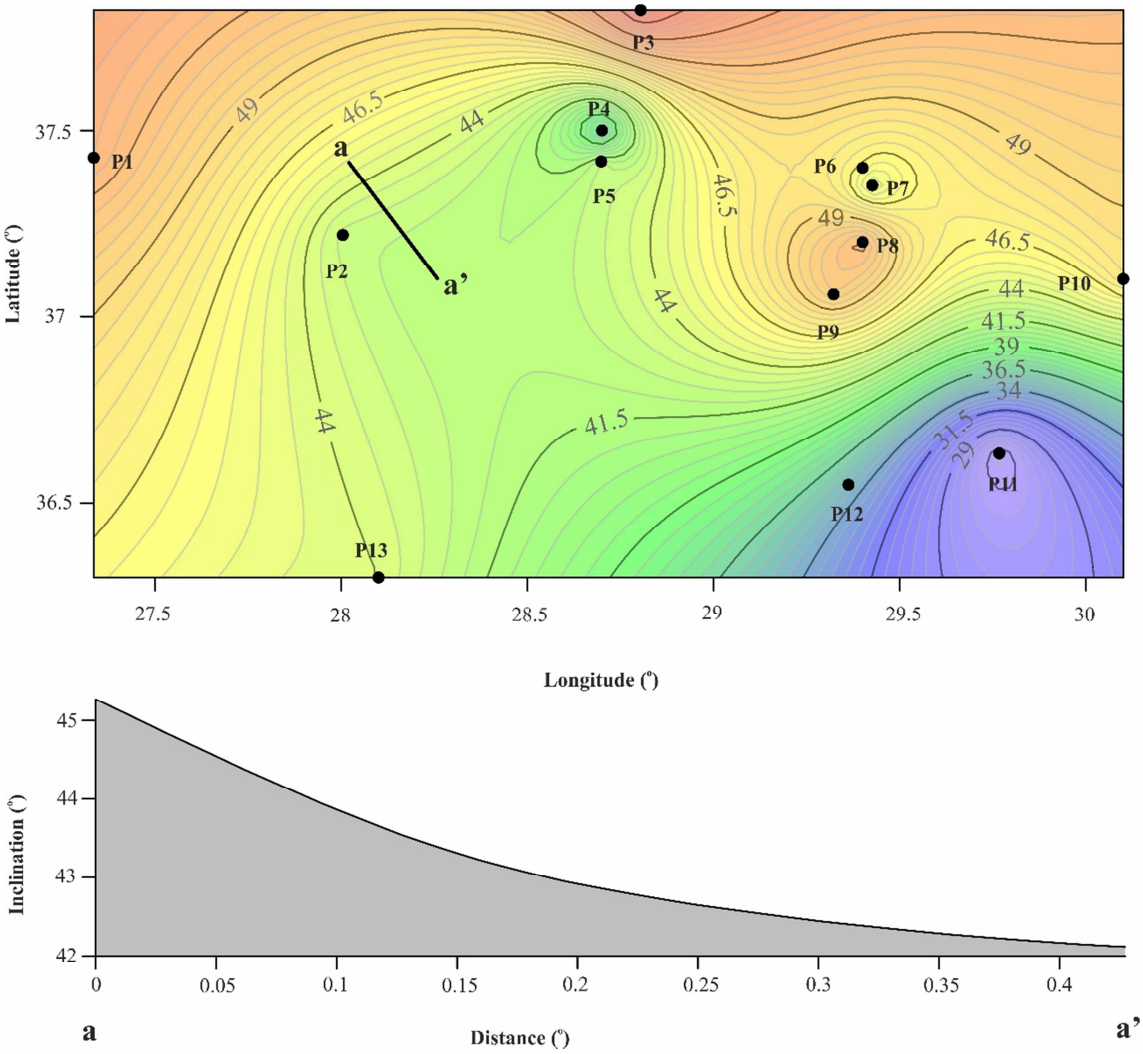

Figure. S5. (a) Projected tilt corrected paleomagnetic inclination values of the SW Anatolia Domain (inclination degrees and station data compiled from Kaymakcı et al., 2018). Small black dots (P) indicate studied sites; besides, contour lines show calculated inclination angles in degree mainly in Neogene period (please review Kaymakcı et al., 2018 for more information regarding the paleomagnetic investigations). Each contour line depicts 0.5 interval of tilt corrected inclination variation. Solid black line represents the location of cross section that virtually run through the orientation of the Yatağan Fault. (b) cross section indicates the variation of inclination degree along with distance from the north west towards the south eastern margin of the basin.